Astronomical tuning for the upper Messinian Spanish Atlantic margin: Disentangling basin evolution, climate cyclicity and MOW

van den Berg, Bas C.J.[a,*], Sierro, F.J.[a], Hilgen, F.J.[b], Flecker, R.[c], Larrasoaña, J.C.[d], Krijgsman, W.[e], Flores, J.A[a]., Mata M.P.[f], Bellido Martín, E.[f], Civis, J.[f], González-Delgado, J.A.[a]

[a]Departamento de Geologia, Facultad de Ciencias, Universidad de Salamanca, 37008 Salamanca, Spain
[b]Stratigraphy/Paleontology, Faculty of Geosciences, Utrecht University, Budapestlaan 4, 3584 CD Utrecht, the Netherlands
[c]School of Geographical Sciences and Cabot Institute, University of Bristol, Bristol, UK
[d]Instituto Geológico y Minero de España, Unidad Zaragoza, Zaragoza, Spain.
[e]Paleomagnetic laboratory "Fort Hoofddijk", Budapestlaan 17, 3584 CD Utrecht, the Netherlands
[f]Instituto Geológico y Minero de España, Rios Rosas 23, Madrid, Spain.

[*]**Corresponding Author:** *Email address*: bvandenberg@usal.es

Abstract

We present a new high-resolution cyclostratigraphic age model for the Messinian sediments of the Montemayor-1 core. This core was drilled in the Guadalquivir Basin in southern Spain, which formed part of the marine corridor linking the Mediterranean with the Atlantic in the Late Miocene. Tuning of high-resolution geochemical records reveals a strong precessional cyclicity, with maximum clastic supply from river run off coinciding with maximum summer insolation. We recognize a gradual change in the nature of the typical cyclic fluctuations in elemental compositions of the sediments through the core, which is associated with a gradual change in depositional environment as the basin infilled. After applying the new age model, the upper Messinian glacial stages and deglaciation are clearly identified in the oxygen isotope records of the Montemayor-1 core. Reinterpretation of existing planktonic and benthic oxygen isotope records for the core and comparison with equivalent successions in the Rifian Corridor in northern Morocco allow the re-evaluation of the influence of the different water masses in

the region: North Atlantic Central Water and Mediterranean Outflow Water. We observe no direct influence of MOW immediately before or during the Messinian Salinity Crisis.

Keywords: Guadalquivir Basin; Messinian Salinity Crisis; Mediterranean Outflow Water; cyclostratigraphy; XRF

1. Introduction

The Messinian Salinity Crisis (MSC, Hsü et al., 1973; Krijgsman et al., 1999; Roveri et al., 2014) is one of the most dramatic events in recent geological history. In less than 700 kyr, the Mediterranean basin accumulated a succession of evaporites more than a kilometre thick as a consequence of the near-complete disconnection of the Mediterranean Sea from the Atlantic Ocean (Ryan, 2009). There is general consensus that the Atlantic Ocean was the water source that provided the chemical components needed for evaporite precipitation. However, the exact location and configuration (e.g. Simon and Meijer, 2015) of the marine gateway(s) that connected the Messinian Mediterranean with the Atlantic during the MSC remains elusive.

As a direct result of the gateway evolution, a number of modelling studies suggest that the Mediterranean Outflow Water (MOW) must have been active during the Early Messinian, but became weaker around 5.97 Ma, with the onset of the MSC and the precipitation of stage 1 primary gypsum (CIESM, 2008). It stopped completely at 5.55 Ma during the halite precipitation, i.e. the MSC acme (Krijgsman and Meijer, 2008; Meijer, 2006). Subsequently, the most commonly accepted model is that, at the Miocene-Pliocene boundary, the Zanclean deluge reconnected the Mediterranean with the Atlantic and re-established MOW through the Gibraltar Strait (e.g. Hsü et al., 1973; Roveri et al., 2014). However, other research based on the presence of marine fauna in the western and central Mediterranean, that is thought to be late Messinian in age, supports a marine reflooding event during the latest Miocene (Bourillot et al., 2010; Braga et al., 2006; Riding et al., 1998). Integrated Ocean Drilling Program (IODP)

expedition 339 planned to investigate the evolution of Atlantic-Mediterranean water exchange from the Messinian to the Holocene close to the Gibraltar Strait in the Gulf of Cádiz (Fig. 1). In order to establish whether MOW was active or not and how it changed during the MSC, a number of sites both offshore (e.g. IODP Site U1387; Fig. 1) in the Gulf of Cádiz (van der Schee, in prep) and onshore (e.g. the Montemayor-1 core; Fig. 1) in the western part of the Guadalquivir Basin (this study), have been investigated.

During most of the Miocene, exchange with the Atlantic occurred through the Betic and Rifian corridors, located in southern Spain and northern Morocco, respectively (Fig. 1). To reconstruct the changes in flow patterns within, and the evolution of these corridors, well-dated reference sections at both ends of each corridor are required. These exist for the Rifian corridor, where the Ain el Beida (Krijgsman et al., 2004) and Loulja (Van der Laan et al., 2006) sections on the Atlantic margin, and the Melilla (Van Assen et al., 2006) and Zobzit (Krijgsman and Langereis, 2000) sections at the Mediterranean side have been astronomically tuned. For the Betic corridors, the Sorbas Basin (Krijgsman et al., 2001; Sierro et al., 2001) serves as a reference section on the Mediterranean margin, but a well-dated reference section at the Atlantic end of the Betic Corridor is currently lacking. The best region for establishing such a reference section is the Guadalquivir Basin (Fig. 1), which formed the connection between the Atlantic Ocean and all of the strands of the Betic corridor to the east and south (Martín et al., 2014). A well-dated section in the Guadalquivir Basin could constrain the role of the Betic Corridor and evolution of MOW during the MSC. Unfortunately, outcrops exposing long sedimentary sequences in this basin are virtually non-existent because of the low lying, heavily vegetated landscape. Therefore we are reliant on subsurface data.

The Montemayor-1 core was drilled in the northwest of the Guadalquivir Basin. Using this borehole, various paleoenvironmental studies, based on benthic foraminifera, environmental magnetism, stable isotopes and pollen analyses have investigated climate, vegetation and sea

level changes during the Messinian, and the possible influence of MOW (Jiménez-Moreno et al., 2013; Larrasoaña et al., 2014; Pérez-Asensio et al., 2012b; 2012a; 2013; 2014). These results show that the Guadalquivir Basin shallowed before, during, and after the MSC. They also suggest that two major cold periods and associated sea level falls took place, one of which is thought to contribute to the onset of the MSC (Pérez-Asensio et al., 2013). Pérez-Asensio et al. (2012b) also suggested that the termination of MOW is recorded in the Montemayor-1 core at 6.18 Ma, and related this event to the closure of the Guadalhorce Corridor. The existing age models of the Montemayor-1 core on which these results are based use magnetobiostratigraphic tie-points (Larrasoaña et al., 2008; 2014) and the correlation of the oxygen isotope record to other, astronomically dated, isotope records in the Atlantic Ocean (Pérez-Asensio et al., 2012b). However, the identification of the marine isotope stages remains uncertain because of both the lack of high-resolution biostratigraphic age control in the critical interval above the C3A.1n–C3r reversal boundary and inconsistencies observed in the pattern of the benthic $\delta^{18}O$ record. The shift to lighter values above the distinct pair of $\delta^{18}O$ maxima identified as stages TG20 and TG22 by Pérez-Asensio et al. (2012b) is particularly inconsistent with the open ocean $\delta^{18}O$ record. Here we aim to improve the age model for the Montemayor-1 core, and evaluate the implications of this new age model for the interpretation of previously published records.

Astronomically induced changes in the amount of insolation result in cyclic changes in climate and therefore in cyclic sedimentary successions (Milankovitch, 1941; Strasser et al., 2006). This provides a powerful tool for constructing high-resolution chronologies. Our new age model is constructed using cyclostratigraphic analysis and tuning of high-resolution geochemical records combined with planktonic foraminiferal astrobiochronology. A similar approach was used for the Ain el Beida and Loulja sections in northern Morocco (Krijgsman et al., 2004; Van der Laan et al., 2006), which are equivalent in age and setting as the Montemayor-1 core (i.e. on the Atlantic margin of a foreland basin), and will therefore be referred to in this paper for

88 comparison. In constructing an astronomically tuned reference section for the Atlantic side of
89 the Betic corridor, we are able to link major changes in the sedimentary succession of the
90 Guadalquivir Basin to local, regional and global events. A number of paleoceanographic proxies
91 can subsequently be used to reconstruct hydrological changes in the Atlantic margins and
92 assess the influence of MOW.

93 ## 2. Geological setting and core

94 The Guadalquivir Basin was formed in the Late Serravallian – Early Tortonian and evolved from
95 foredeep to foreland basin throughout the Miocene by downward flexure of the basin as a
96 response to loading of the imbricated Betic External units (Berástegui et al., 1998; García-
97 Castellanos et al., 2002; Sanz de Galdeano and Vera, 1992; Sierro et al., 1996). The basin is
98 bounded by the Iberian massif to the North, the subbetic thrust belt of the Betic Cordillera to
99 the south, and is open to the Atlantic Ocean at its western end (Fig. 1). It has experienced
100 continuous sedimentation from middle-late Miocene up to the late early Pleistocene
101 (González-Delgado et al., 2004; Salvany et al., 2011; Sierro et al., 1996). After the closure of the
102 Betic corridors, the Guadalquivir Basin developed as an embayment to the Atlantic, gradually
103 filling up from east to west, in a configuration that persists today in the Gulf of Cádiz.

104 The Montemayor-1 core was drilled in November 2001 near the village of Moguer in the
105 northwest Guadalquivir Basin at 37°15.99'N; 6°48.62'W (Fig. 1). The core recovered marine
106 sediments that correspond to the four lowermost lithostratigraphic units of the basin infill (Fig.
107 2; Sierro et al., 1996). The lowermost unit, the Niebla Formation, is Tortonian in age and
108 consists of a mix of calcareous and siliciclastic sediments deposited during the marine
109 transgression over the Paleozoic-Mesozoic basement. The middle unit, the Arcillas de
110 Gibraleón Formation, covers the largest part of the borehole. It is Tortonian-Messinian in age
111 and consists of nearly-continuous homogeneous bluish-green clays with some interbedded
112 silty beds and a glauconite layer at its base (~252 mcd). This formation is the main focus of this

113 study. Above this unit is the Arenas de Huelva Formation, which consists of lower Pliocene
114 sands, with a pronounced glauconite layer at the base of the formation, at about 60 meter
115 core depth (mcd). This unit is overlain by the transitional sands of the Arenas de Bonares
116 Formation (Larrasoaña et al., 2008; 2014).

117 Based on the age model of Larrasoaña et al. (2008), the normal polarity chron observed at the
118 top of the core (labelled N5) begins within the glauconite layer (Fig. 2). As glauconite typically
119 forms during periods of very slow or negligible marine sedimentation, this glauconite layer
120 probably corresponds to a condensed interval or hiatus (e.g. Jiménez-Moreno et al., 2013). If
121 we examine closely the magneto- biostratigraphic results, bio-event 4 (Sierro et al., 1993) and
122 the top of chron C3An.2n are found at almost the same core depth (237 mcd and 238 mcd,
123 respectively), although these events are clearly separated in the Ain el Beida section and the
124 GTS with an age difference of 70 kyr (Krijgsman et al., 2004; Lourens et al., 2004). Therefore
125 this interval must also be condensed or associated with a (small) hiatus in this part of the core.
126 In order to assess the cyclicity, continuous sedimentation is required. Consequently we will
127 only consider the interval 60-237 mcd (Fig. 2) which spans ca. 6.4-5 Ma (Larrasoaña et al.,
128 2008; 2014) capturing the entire duration of the MSC (5.97-5.33 Ma; Roveri et al., 2014).

129 # 3. Method

130 ## 3.1 X-Ray Fluorescence (XRF) analyses

131 The strikingly homogeneous composition and lithology that dominates the Montemayor-1 core
132 (Fig. 2), prevents the construction of a reliable cyclostratigraphic framework based on visually
133 identifiable lithological cycles (e.g. grain size and lithology). Cyclic changes may, however, be
134 apparent in the chemical composition of the sediments. To detect these, we measured a total
135 of 527 samples using X-Ray Fluorescence (XRF) with a NITON XL3t900 GOLDD analyser.
136 Measurements were done in 'mining Cu/Zn' mode, measuring time was 150 seconds per

sample and Helium purging was used for optimal detection of light elements. The hand-held analyser was used while placed in its holder and the analyses were done on three different sample surfaces, which were smoothed and flattened using a scalpel. One sample was selected as a 'standard' and measured several times during the entire measurement campaign to be able to detect measurement anomalies or gradual deviations over time. Analysis of this standard data did not indicate any measurement inconsistencies. All samples were measured three times and the reproducibility was in general good with very few outliers. Since the clays forming the matrix throughout the entire studied section are very homogenous (except for the very top), anomalies due to changes in the matrix are not expected.

The use of fast, low-cost XRF methods is increasingly used for chemostratigraphy and/or geochemical shifts in sedimentary records. XRF core-scanning measurements have been widely applied when a well-preserved section is available. Validation and discussion of this method can be found in Jansen et al. (1998); Richter et al. (2006); Tjallingii et al. (2007). The reliability of geochemical data obtained from handheld XRF devices has been demonstrated previously, in both the field and laboratory data (Higueras et al., 2012; Kalnicky and Singhvi, 2001; Rowe et al., 2012; USEPA, 2006).

To assess the reliability of our data still further, we performed an additional calibration for the data obtained by the NITON XL3t900 GOLDD analyser using a conventional WD-XRF of the Instituto Geológico y Minero de España (IGME). For this calibration, major and trace element concentrations were determined by WD-XRF analysis using a MAGIX PANalytical equipped with an Rh x-ray tube at 2.4 Kw. Quantitative data were obtained using superQ PANalytical software. Major elements were measured on a lithium borate-fused disk (Spectromelt A1000, 0.3 g sample: 5.5 g flux) to avoid matrix effects typical of sediments and rocks. Trace elements were determined in a pressed powder pellet, with elvacite as a binding agent, and quantitative

161 data were obtained with pro-trace software, which includes chemical matrix effects correction,
162 interference of spectral lines and background corrections.

163 Figure 3 shows the correlation plots for the three most important major elements, based on
164 Principal Component Analysis loadings (see section 4.1): Calcium (R^2=0.78), Silicon (R^2=0.70)
165 and Titanium (R^2=0.78), and the three trace elements used in this study: Strontium (R^2=0.96),
166 Zirconium (R^2=0.77) and Rubidium (R^2=0.88) for a selection of 31 samples selected from the
167 entire core. Only Silicon seemed to be largely influenced by the change in matrix at the bottom
168 and top of the core, therefore for this element only the samples of the interval of
169 homogeneous bluish-green clays used in this study are used. These correlations indicate that
170 although the absolute values of element concentrations obtained with the NITON handheld
171 analyser should be treated with caution, the relative changes in geochemical composition are
172 robust.

173 ### 3.2 Statistics

174 Dixon's test (Dean and Dixon, 1951; Rorabacher, 1991) was used to detect outliers with 95%
175 confidence. Outliers were excluded and the remaining values were averaged for each sample.
176 A well-known problem with XRF measurements is that lighter elements emit a smaller signal
177 when excited and their emission is therefore more prone to attenuation (Tjallingii et al., 2007).
178 In order to account for the larger scattering of light elements like aluminium and silicon, only a
179 three-point average of these measurements has been used (Fig. 4). Likewise, elements with
180 very low concentrations (less than 100 ppm), in this case only rubidium, are subjected to
181 enhanced scattering and consequently only a three-point average of this record has been used
182 (Fig. 4). Since aluminium yields enhanced scattering, the common practice of Aluminium
183 normalization will not be applied here. Instead, as proposed by Davis and Sampson (2002) and
184 Aitchison (1986) we performed a centred log-ratio transformation, to make the dataset 'open'
185 (i.e. remove all spurious correlations), and statistically robust. This involves dividing through

186 the geometric mean, which is a type of normalization (Aitchison, 1986; Davis and Sampson,
187 2002), allowing direct comparison between the major oxides and trace elements. A centred
188 log-ratio transformation also allows each of the elements to be represented in the Principal
189 Component Analysis (PCA), which was conducted using the PAST version 3.01 software
190 package (Hammer et al., 2001). Note that when using any element as a common denominator,
191 this element cannot be considered further when performing PCA.

192 # 4. Results

193 ## 4.1 Principal Component Analysis

194 All elements measured and used in this study are presented in figure 4 and the data is added
195 as supplementary data. Principal component analysis was performed to simplify and visualize
196 the data matrix. Elements with similar behaviour are combined into a few components, each
197 of which represents a specific linear combination of elements, in such a way that the linear
198 combination of the first principal component explains the largest possible amount of variance
199 within the dataset. Subsequently, the second component explains the largest possible amount
200 of the remaining variance, and so on (Davis and Sampson, 2002). This analysis yields two
201 statistically significant components: the first principal component (PC1), describing 51% of the
202 total variance and the second principal component (PC2) describing 37% of the total variance
203 (table 1). The two most important negative loadings for PC1 are Ca and Sr (Fig. 5), while the
204 positive loadings comprise Zr, Si, Ti, K and Fe (in descending order). For PC2, the two most
205 important positive components are Zr and Ca. The negative loadings consist of Fe, Al, Rb, and K
206 (Fig. 5). All elements that have a positive loading for PC1 are important components of
207 aluminosilicate minerals. Ca and Sr are the major elements in biogenic carbonate, which visual
208 inspection suggests is mainly associated with foraminifera and coccoliths. The relationship
209 between the loadings of PC2 is unclear. Both the XRF and the PCA data is included as
210 supplement file

4.2 Geochemical records in depth domain

PC1 (Fig. 2) shows regular alternations, gradually thickening upwards, with a sudden increase in thickness around 175 mcd. The pattern is very similar to the observed patterns in all the individual element records (Fig. 4). In the bottom part (238-220 mcd), three groups of alternations can be distinguished, each separated by a pronounced minimum. The amplitude of the alternations becomes smaller towards the top of the core, especially above 120 mcd. The sudden increase at the top of the record (above 66 mcd) corresponds to a change in lithology, from clays to sands, just before the glauconite layer.

In addition, to assess the nature of the regular alternations and changes therein, a principal component has been performed on both the lower (70-190 mcd) and the upper (190-237 mcd) part separately. The PC1 records of both intervals show identical regular alternations as the PC1 of the entire core. However, surprisingly, the loadings comprising these alternations change from the lower to the upper interval (Fig. 5). The first principal component of the lower part (PC1L) shows similar loadings to PC1, with Ca and Sr being the most important elements on the negative side and the aluminosilicates at the positive side, only the contribution of Zr to PC1U is negligible in comparison to PC1. The first principal component for the upper part of the record (PC1U), however, consists of a very different combination of loadings. Here the most important positive loading is Zr, followed by Ti and Si, while the negative side consists predominantly of Ca followed by K, Fe and Rb which are commonly associated with clay minerals.

The benthic $\delta^{18}O$ record of the Montemayor-1 core (Fig. 6; Pérez-Asensio et al., 2012b) also shows regular alternations, with heavier values common in the 200-175 mcd interval and a sudden increase in thickness at 175 mcd. The top part of the $\delta^{18}O$ record (above 175 mcd) is in anti-phase with PC1. Below 175 mcd there is no clear phase relation. This could be due to the lower resolution of the record.

5. Age model

5.1 New biostratigraphic events

In order to build a more accurate biostratigraphic framework, we analysed and counted the keeled Globorotaliids, in particular changes in abundance of *Globorotalia margaritae* and *Globorotalia menardii* sin (Fig. 7, supplementary data). For the 170-180 mcd interval, where possible, 400 specimens per sample were counted, because in this interval the two influxes of *G. menardii* sin were identified which have a relatively low abundance (2-8%), the other intervals were extensively scanned to assure no influxes were missed. For the interval below 180 mcd, 100 specimens per sample were counted to reconstruct the acme of *G. margaritae* which has a much higher abundance (15-35%) and therefore 100 specimens per sample is sufficient to give a reliable representation. To justify this, the 95% confidence interval based on the binomial standard error (Dennison and Hay, 1967; Fatela and Taborda, 2002) is also plotted in figure 7, clearly showing the reliability of the two influxes of *G. menardii* as well as the acme of *G. margaritae*. Changes in abundance of these two species have been linked to specific astronomical cycles in the Ain el Beida and Loulja sections (Krijgsman et al., 2004; Van der Laan et al., 2006). Two influxes of *Globorotalia menardii*, found in Ain el Beida cycle 42 (5.55 Ma) and cycle 43 (5.53 Ma; Krijgsman et al., 2004, Fig. 2) and in the bottom of the Loulja section (Van der Laan et al., 2006), were recorded in the Montemayor-1 core at 176 and 172 mcd, respectively (Fig. 7). These two influxes of *G. menardii* sin were erroneously reported in Ain el Beida as *Globorotalia miotumida* (Krijgsman et al., 2004; Tulbure et al., in prep).

Two intervals of abundant *G. margaritae* are found in the 210-198 mcd interval, with a brief low abundance interval at 199.1 mcd (Fig. 7). Another short peak is found at 185.6 mcd. The two intervals with abundant *G. margaritae* may coincide with the *G. margaritae* acme at Ain el Beida which also shows two peaks in abundance, in cycles 33 and 35 (Krijgsman et al., 2004), corresponding to glacial stages TG20 and TG22.

For the 244-234 mcd interval, up to 40 specimens of *Neogloboquadrina acostaensis* were counted to estimate the sinistral to dextral ratio in order to confirm the depth of the main sinistral to dextral coiling change (Fig. 7). This marks the bottom end of the record analysed in this study.

5.2 Cyclostratigraphic age model.

To perform a cyclostratigraphic study of the geochemical records we first need to demonstrate that the alternations in the geochemical record are of astronomical origin, corresponding to the periods of precession, obliquity and/or eccentricity. To demonstrate this we used the depths and astronomical ages of the two bio-events that are furthest apart, together with the number of geochemical alternations between them. Between the coiling change of *N. acostaensis* (bio-event 4, 6.37 Ma) and the highest influx of *G. menardii* (5.53 Ma), which covers a time span of ~840 kyr, we identified ca. 38 cycles (Fig. 6). This means each cycle has an average period of ~22 kyr, which coincides well with the average precession period.

Next we have to understand the nature of the geochemical cycles based on the PCA loadings and the phase relation with respect to the astronomical target curve. Since both the PCA loadings and the phase relation changes along the core, we will first consider the cycle nature, phase relation and subsequent tuning for individual parts of the record before interpreting the evolution of the record as a whole. In general, based on the loadings of the principal components (Fig. 5), PC1 as well as PC1L can both be considered as representing the juxtaposition of biogenic carbonate versus aluminosilicates (clay). In Ain el Beida, the same relationship is found for PC1, where maxima of fine grained aluminosilicates are found in the red layers, and minima in the beige layers (Van der Laan et al., 2012). At Ain el Beida, this is explained by terrigenous, fluvial influx of aluminosilicates into the basin during wet periods causing dilution of the biogenic carbonate content. The red layers with low carbonate content correspond to precession minima and summer insolation maxima, as they share many proxy

signals with Mediterranean sapropels, while the beige layers with high carbonate content correspond to precession maxima and summer insolation minima.

Again, based on the loadings, our PC1U can be considered as a proxy for grain size of terrigenous particles, with Zr, Si and Ti on the positive axis typically representing the silty fraction, while the elements accompanying Ca on the negative axis are typically found in the clay fraction (Fig. 5). This relationship is confirmed by grain size measurements carried out on 38 samples from the upper part of the core, yielding a positive correlation between PC1U and UP10 (R^2=0.6727, P_{uncorr}= $3*10^{-10}$; Fig. 8). The UP10 size (i.e. the percentage of the sample consisting of particles coarser than 10 μm), which adds the fine sand subpopulation to the sortable silt size fraction (10-63 μm), is considered a proxy for paleocurrent intensity (McCave et al., 1995). Even though the correlation is clear, the R^2 value is not so high, probably due to the relative small number of samples. In conclusion, while PC1L shows the biogenic carbonate versus clay ratio, PC1U reflects the biogenic carbonate and clay versus silt ratio.

5.2.1 Tuning of the lower interval (238-210 mcd)

Based on the phase relation described above, we correlate insolation minima to maxima in calcium carbonate in the Montemayor core. Since calcium has a negative loading on PC1, we tune PC1 minima to insolation minima, and PC1 maxima to insolation maxima (Fig. 6).

Our results are tuned to the $La2004_{(1,1)}$ solution (Laskar et al., 2004). The first order calibration involves tuning to eccentricity. Intervals with higher amplitude peaks should correspond to eccentricity maxima. In the depth domain, PC1 yields five intervals with high amplitude maxima (at 234, 228, 222, 218 and 211 mcd) which, based on the initial magnetobiostratigraphic age model (Larrasoaña et al., 2008), should correspond to the five ~100-ka eccentricity maxima between 6.37-5.88 Ma. The tuning is constrained by normal chron C3An.1n, the base of which is located at 232 mcd, just above the oldest of the five intervals with high amplitude variability in PC1, and the top at 218 mcd, just below the fourth

311 interval (Fig. 6). The prominent maxima in the PC1 curve just below the base of C3An.1n
312 should therefore be tuned to the four precession related peaks associated with the ~100-ka
313 eccentricity maximum at 6.3 Ma. The three prominent maxima in the lower part of chron
314 C3An.1n are tuned to the three precession related peaks in the eccentricity maximum at 6.2
315 Ma, while the four maxima in the upper part of this chron are tuned to precession related
316 peaks in the eccentricity maximum around 6.1 Ma. This tuning to eccentricity is continued for
317 the two youngest intervals with high amplitude variations located above C3An.1n. The small
318 peaks flanking the prominent peak in PC1 at 6.1 Ma should also represent precession related
319 cycles and thus correspond to precession driven insolation maxima. As shown by Van der Laan
320 et al. (2005), sedimentation rates at Ain el Beida can be up to five times higher in the thickest
321 and most prominent reddish marl layers as a consequence of the high amplitude insolation
322 maxima and precession minima at times of maximum eccentricity. This can be explained by
323 much-enhanced fluvial runoff and associated sediment supply during extreme insolation
324 maxima. This link between sedimentation rate and the amplitude of precession, or more
325 correctly, the amplitude of precession minima and, hence, summer insolation maxima, may
326 explain the expanded thickness of high amplitude PC1 cycles while less pronounced cycles
327 remain thin.

328 ***5.2.2 Tuning of the upper interval (60-178 mcd)***

329 The PC1 and PC1U records in this interval are almost identical (Fig. 2), but each is based on a
330 different set of loadings (Fig. 5). Since the loadings of PC1U must, by definition, represent this
331 interval best, we will use these to explain the nature of the cycles. Maxima in carbonate now
332 correspond to maxima in clay since carbonate and the clay minerals are found on the same
333 side of the loadings axis. To evaluate the phase relation of these cycles with respect to
334 insolation, we use the bio-events and the $\delta^{18}O$ record of Pérez-Asensio et al. (2012b). At Ain el
335 Beida, the two influxes of *Globorotalia menardii* are found in successive beige layers and thus
336 correspond to insolation minima. In our record these influxes coincide with PC1 maxima, which

should therefore also correspond to insolation minima. This suggests that PC1's phase relationship with precession in the upper interval is different from its relationship with precession in the lower interval (Fig. 6). This is confirmed by the benthic $\delta^{18}O$ record, which shows clear alternations in the upper part of the record where minima in the benthic $\delta^{18}O$ record are in phase with minima in PC1. Both the $\delta^{18}O$ record of Ain el Beida (Krijgsman et al., 2004) and the lower part of the Loulja $\delta^{18}O$ record (Fig. 9; Van der Laan et al., 2006) show clear precession-related cyclicity with minima in $\delta^{18}O$ corresponding to maxima in insolation. Therefore we also expect minima in the benthic $\delta^{18}O$ record of the Montemayor-1 core to correspond to maxima in insolation.

Unfortunately, as a result of the condensed glauconitic interval there is no reliable bio- or magnetostratigraphic tie point at the top of the record. However, since the geochemical alternations in the lower interval are invariably controlled by precession, we interpret the clear cycles in the upper interval to be precession related as well. This is confirmed by the bio-events and the benthic $\delta^{18}O$ record. Influxes of *Globorotalia menardii,* which are expected in successive precession maxima (Krijgsman et al., 2004; Lourens et al., 2004), are found in successive PC1 maxima. The benthic $\delta^{18}O$ record of Loulja (Van der Laan et al., 2006) has a strong precessional component for the influxes of the *Globorotalia menardii* interval and above. Likewise, the alternations in the upper interval of the Montemayor-1 benthic $\delta^{18}O$ record, in phase with PC1, should also be controlled by precession. Finally, if the alternations were related to obliquity the precessional component should still be, at least partly, distinguishable, e.g. see the benthic $\delta^{18}O$ records of Ain el Beida and Loulja (Van der Laan et al., 2005; 2006). However, the cycles in de PC1 as well as in the $\delta^{18}O$ record are very simple, i.e. there is no indication of interference patterns derived from both precession and obliquity. This all suggests that the cycles in the upper interval are precession related. Unfortunately, there is no clear eccentricity related pattern in this part of the record that would strengthen

362 the tuning. Only the last complete alternation at the top is substantially thicker; this cycle is
363 tuned to the eccentricity minimum at 5.38 Ma.

364 If the cycles are precessional and are used to constrain the age of the succession, the base of
365 the glauconite layer at the top of our record corresponds exactly with the Miocene–Pliocene
366 boundary (5.33 Ma; Fig. 6). Since the base of chron C3n is dated at 5.235 Ma (Fig. 2; Lourens et
367 al., 2004), and assuming that polarity interval N5 correlates with chron C3n.4n (see Larrasoaña
368 et al., 2008), this implies a condensed interval of at least 100 kyr, associated with the
369 glauconite layer.

370 ***5.2.3 Tuning of the middle interval (210-178 mcd)***

371 The tuning of the middle interval is more complicated as the signal amplitude is low and the
372 observed change in cycle nature, expressed by the change in PCA loadings, takes place here.
373 This change is gradual and it is therefore not possible to pinpoint its exact location. To
374 calculate PC1L and PC1U we have set the division between the lower and upper interval at 190
375 mcd. Since we want to assess the nature of the patterns, and the patterns in PC1L and PC1U
376 are very similar to the ones found in respectively the lower and upper interval of PC1, this
377 division is justified. For the top part of this middle interval (190-178 mcd), apart from some
378 details, the general pattern in PC1U is the same as in PC1. Therefore, just like the upper
379 interval, we will tune PC1 minima to insolation maxima. The insolation curve for this part is
380 characterized by a 400 kyr eccentricity minimum, resulting in low amplitude precession cycles.
381 As a result, not all cycles are expressed in the record. In addition, very few samples were
382 available for XRF measurements in the 195-189 mcd interval, so the data resolution is too low
383 to demonstrate a clear pattern. Both the low amplitude of the signal and the low sample
384 resolution hamper a straightforward tuning, resulting in only a best possible fit for this part of
385 the record. If we assume no major changes in sedimentation rate, at least two cycles are either
386 missing or are not expressed in the 195-189 mcd interval. By also assuming that the low

amplitude precession cycle, which is not expressed as a reddish layer above cycle 38 at Ain el Beida (Krijgsman et al., 2004), is not well expressed in the Montemayor core either, we can then tune the remaining alternations to the remaining precession cycles in this upper part of the middle interval. Due to all these uncertainties, this part of the tuning is marked with dashed lines in figure 6, and an extra uncertainty of one precession cycle (22 kyr) must be taken into account.

In the bottom part of this interval (190-210 mcd), the cycles are not so well expressed as in the lower interval of the entire core. However, the pattern of PC1 and PC1L is nearly identical for this interval, so we interpret that the nature of the cyclicity is the same and maxima in PC1 and PC1L should be tuned to insolation maxima (Fig. 6).

6. Discussion

6.1 Comparison with previous age models

The first age model was constructed by Larrasoaña et al. (2008), based on bio- and magnetostratigraphic tie points. Subsequently, Pérez-Asensio et al. (2012b) changed this age model by attempting to identify glacial stage TG22. We have improved the age model by adding extra biostratigraphic tie-points; the two influxes of *G. menardii* and the *G. margaritae* acme (Fig. 6). These tie-points suggest that a reinterpretation of the $\delta^{18}O$ record is required. The two heavy excursions in the $\delta^{18}O$ record, at 176 and 183 mcd, should be correlated to isotope stages TG12 and TG14 (Fig. 6), and not to TG20 and TG22 as proposed by Pérez-Asensio et al. (2012b). Consequently only two other maxima, i.e. at 193 and 199 mcd, remain candidates for isotope stages TG20 and TG22. This is confirmed by the *G. margaritae* acme (Fig. 6), which corresponds to the same glacial stages at Ain el Beida (Krijgsman et al., 2004). The acme of *G margaritae* was not used to construct the age model and therefore confirms independently our tuning.

As a consequence of the successfully tuning of the PC1 record, the uncertainty associated with the age model has been reduced to only a couple of thousands of years, except for the interval between 5.7-5.6 Ma where, due to the tuning issues addressed in section 5.2.3, an extra uncertainty of one precession cycle must be taken into account.

6.2 Mechanisms driving sedimentary cycles

6.2.1 Lower interval (238-210 mcd; 6.37-5.9 Ma)

The geochemical cycles of the lower interval (Fig. 6) are mainly driven by precession forced cyclical changes in annual rainfall with more biogenic carbonate concentrated at times of Northern Hemisphere summer insolation minima when terrigenous supply is low. By contrast, enhanced amounts of terrigenous sediments, which in a distal setting are dominated by clays, are deposited at times of Northern Hemisphere summer insolation maxima when high rates of annual rainfall resulted in enhanced clay supply to the Guadalquivir Basin through intensified river run off. Plumes of fine-grained terrigenous material will dilute the biogenic carbonate-rich sediments. As a consequence, the sedimentary cycles are expressed by the regular alternations of carbonate-rich, more silty beds and carbonate-poor, clay rich layers, similar to those described in other Atlantic sections like Ain el Beida (Van der Laan et al., 2012) and Loulja (Van der Laan et al., 2006).

Similar astronomically-driven cyclical changes in gamma-ray and sonic logs have been recorded in the Gulf of Cádiz during the Pliocene (Sierro et al., 2000). High annual rainfall in southern Spain at times of maximum summer insolation resulted in enhanced detrital supply to the Gulf of Cádiz and deposition of clay-rich beds with high gamma ray and sonic values, while dryer climates at times of minimum insolation correspond to low gamma ray and sonic values. Iberian margin piston cores taken in the Atlantic Ocean also yield colour cycles that can be linked to precession (Hodell et al., 2013). These authors explain the precession-induced changes in sediment redness and alcohol ratios by changes in wind-driven processes (e.g. dust

436 transport, upwelling or precipitation). However, a logical alternative explanation would be that
437 these cycles are related to fluvial terrigenous input, with enhanced clay input causing
438 increased sediment redness when oxidized. More recent carbonate cycles in cores spanning
439 the last 225-250 kyr, recovered in the Atlantic Ocean off Morocco, share many similarities with
440 the cycles described above (Bozzano et al., 2002; Moreno et al., 2001). Carbonate minima in
441 these sediments show a similar in-phase relation with precession minima, and have also been
442 interpreted as dilution cycles. These authors, like Hodell et al. (2013), attribute the carbonate
443 dilution to an eolian rather than a fluvial source, due to the site location which is relatively far
444 (200 km) from the Moroccan margin but in the pathway of present-day Saharan dust plumes.
445 However, as stated by Van der Laan et al. (2012), the luminescence ages (von Suchodoletz et
446 al., 2008; 2010) do not exclude an alternative interpretation with wetter periods
447 corresponding to precession minima and yielding a perfect fit with the much better dated last
448 wet phase on Lanzarote between 15 and 8.5 kyr (e.g. Damnati et al., 1996; see von
449 Suchodoletz et al., 2010). This phase, centered around the last precession minimum at 11-12
450 kyr, is consistent with our interpretation of carbonate minima being related to carbonate
451 dilution caused by enhanced river runoff. When considering all these sections and sites, this
452 kind of cyclicity is clearly not restricted to the Messinian Guadalquivir Basin, but found
453 throughout the entire recent geological history and in at least the entire Mediterranean and
454 the neighbouring Atlantic region.

455 ***6.2.2 Upper interval (178-60 mcd; 5.53-5.33 Ma)***

456 The Principal Component Analyses show an up core change from biogenic carbonate versus
457 clay cycles (PC1L) to cycles of biogenic carbonate and clay versus silt (PC1U, Fig. 5). On top of
458 that, the records show an increase in sedimentation rate at around 180 mcd that is
459 demonstrated by a clear increase in the thickness of the precession cycles, followed by a
460 gradual increase in PC1U from 175 mcd to the top, reflecting a coarsening-upward
461 sedimentary sequence (Fig. 2). Lastly, this interval coincides with an observed decrease in

462 paleodepth from 400 to 100 meter (Pérez-Asensio et al., 2012a). All these features are
463 consistent with a gradual east-west infilling of the Guadalquivir Basin in the late Miocene
464 (Iribarren et al., 2009; Sierro et al., 1996). The change in lithology and sedimentation rate at
465 180 mcd may reflect the transition from a more distal, deeper water environment to a
466 shallower, more proximal one, probably associated with prodelta progradation and rapid
467 infilling of the basin.

468 In this upper interval sedimentary cycles also seem to be driven by regular alternations in the
469 rate of terrigenous supply to the basin. However, because of the proximity to the coast, the
470 grain size of detrital particles is dominated here by silts in contrast to the clay rich deposits
471 that characterize the lower part. In consequence, phases of higher input of silt material from
472 the shelf dilutes the biogenic carbonate and clay, while a decrease of this coarser grained
473 detrital supply would lead to a relative increase of the biogenic carbonate and clay
474 component. This suggests that the relationship between local climate and detrital input is
475 strongly affected by the distance to the coast. Distal marine settings can only be reached by
476 the clay fraction that is transported in suspension far away from the coast, whereas coarser
477 particles, such as silts or sands, remain on the shelf, and dominate the detrital input in more
478 proximal settings.

479 Throughout the entire record detrital supply dilutes biogenic carbonate. However, the phase
480 relationship between carbonate-rich beds and insolation changes from the lower to the upper
481 part. This can be explained by changes in erosion rates. Summer insolation minima cause a
482 colder and more arid climate. This may have a negative effect on the vegetation cover of the
483 Guadalquivir basin. Land with a permanent vegetation cover is characterized by soil losses
484 which are generally more than an order of magnitude lower than those on arable land (Cerdan
485 et al., 2010). Therefore loss in vegetation cover would result in more erosion of the land during
486 insolation minima. This would lead to an increased input of coarser-grained material to the

shelf through increased sediment concentration in the river discharge at times of insolation minima due to more intense erosion of non-vegetated landscapes. Subsequently the core's environment at the outer shelf is reached by these sediments through storms and thereby diluting the biogenic carbonate and the clay during insolation minima, also explaining the concurrent increase in cycle thickness. Meanwhile, river discharge is higher at times of insolation maxima when a wetter climate and a more vegetated landscape prevailed in Southern Spain, however the sediment concentration, and therefore sediment input, was lower and consisted mainly of clays.

A similar mechanism is proposed to explain the cyclic depositional changes in the Plio-Quarternary continental deposits of the Guadix Basin (Pla-Pueyo et al., 2015). These authors explain cyclical changes between alluvial and fluvial deposits to changes in vegetation cover and subsequent erosion. Also, similar climatic dependencies on erosion and alluvial fan progradation have been observed in Nevada and California, USA (Harvey et al., 1999). So far this mechanism has only been attributed to cycles found in continental deposits, but since the setting of the Montemayor core is proximal for the upper interval, we propose that this mechanism can result in similar cyclicity in shallow marine deposits.

Two other models that cannot currently be ruled out can also explain the observed cyclicity. First, it may be the result of enhanced input of detrital, fine-grained carbonate to the basin during insolation maxima adding to the biogenic carbonate component. However since we observe an increase in the number of coccoliths and foraminifera in our samples during insolation maxima, implying that the carbonate is mainly of biogenic origin, this model is unlikely. Another alternative model is based on changes in bottom current strength. Stronger currents during insolation minima would cause winnowing of the fine-grained, lighter, non-cohesive particles, leaving an enriched layer of coarser grained particles and heavier minerals (McCave and Hall, 2006). The most likely candidate for changes in current strength on

precessional timescales in concordance with the phase relation described here is MOW (Kaboth et al., this issue; Lofi et al., this issue). However, as we will conclude in section 6.3, we don't observe any direct influence of MOW on this part of the Montemayor-1 core; therefore also this model is unlikely.

The infilling of the Guadalquivir Basin, and consequently the change in cycle nature, is also supported by fluctuations in benthic foraminifera abundances in combination with the geochemical and oxygen isotope records. In the lower part of the record the coastline is still distant and input of fluvial-derived nutrients and terrestrial organic matter is relatively low, resulting in mesotrophic conditions in which *Uvigerina peregrina s.l.* thrives (Fig. 9; Pérez-Asensio et al., 2012a; 2014 and references therein). As the depositional environment of the sediments of the Montemayor-1 core becomes more proximal, *U. peregrina s.l.* decreases in abundance and *Brizalina spathulata* increases along with *Bulimina aculeata* (Pérez-Asensio et al., 2014). These species are eutrophic, associated with conditions of high degraded organic matter input and low oxygen (Pérez-Asensio et al., 2012a; 2014 and references therein).

In the upper interval of the record we find a clear relationship between insolation, PC1, benthic foraminifera and the oxygen isotopes (dashed lines in Fig. 9). Precession minima are in phase with minima in PC1, relatively low abundances of *U. peregrina s.l.,* high abundances of *B. spathulata*, and light $\delta^{18}O$ values. The main factor driving these phase relationships is arguably changes in sea floor oxygen concentration, due to grain size fluctuations in the sediment input, forced by precession. During insolation minima (precession maxima) decreased vegetation cover leads to relatively high input of coarser-grained sediment. This results in higher porosity and therefore better oxygenated sediments at the seafloor, leading to lower abundance of eutrophic species like *B. spathulata* and higher abundances of *U. peregrina s.l.*, which is living less deep in the sediment and is more dependent on oxygen supply. At the same time, as Pérez-Asensio et al. (2014) argues, stronger winds may cause

upwelling which could also result in an increase in fresh organic matter and also therefore higher abundances of *U. peregrina s.l*. Warm/wet periods during precession minima, on the other hand, will trigger enhanced input of clay (PC1U), leading to lower sediment porosities and therefore oxygen depleted conditions, resulting in higher abundances of *B. spathulata*. We therefore suggest that, in the upper interval where the depositional environment is more proximal, fluctuations in the benthic foraminifera assemblages are largely regulated by precession-related changes in oxygen input through sediment supply instead of glacio-eustatic fluctuations as stated by Pérez-Asensio et al. (2014).

6.3 Reinterpretation of stable isotope records

6.3.1 Stable isotope chronostratigraphy

The new high-resolution chronology allows a very precise correlation of the isotope records of the Montemayor-1 core with other astronomically-tuned isotope records. We focus particularly on comparison with the oxygen isotope records from Ain el Beida (Krijgsman et al., 2004), Loulja (Van der Laan et al., 2006) and Site 982 of ODP Leg 162 (Hodell et al., 2001; Fig. 9 & 10). In general, the benthic $\delta^{18}O$ record of the Montemayor-1 core shows increasingly heavier values up core, culminating in the glacial period of 5.9-5.5 Ma (Fig. 9). The same trend is also found in the planktonic $\delta^{18}O$ record, but is interrupted by a decrease at 5.75 Ma, after TG20. However, this increasing trend is not seen in the benthic $\delta^{18}O$ record from ODP Site 982 or Ain el Beida (Fig. 9). The sudden decrease towards lighter values at 5.53 Ma in the benthic $\delta^{18}O$ record of the Montemayor-1 core coincides well with the deglaciation towards TG11 and finally TG9. This shift is greater than for the benthic $\delta^{18}O$ record of Ain el Beida and the open ocean benthic $\delta^{18}O$ record of ODP Site 982 (Fig. 10), which can be explained by a concurrent decrease in paleodepth (Pérez-Asensio et al., 2012a), generating a shallower and therefore warmer environment. The decrease in paleodepth is confirmed by a decrease in the offset between the planktonic and benthic $\delta^{18}O$ values. In the lower interval this offset is more than 1‰, but declines up core to values less than 0.5‰ (Fig. 9), corresponding to a decrease in

563 temperature difference between bottom and surface waters of 2-3°C. (Shackleton, 1974).
564 Assuming a stabilized vertical temperature gradient, this could correspond to a decrease in
565 paleodepth from 400 to 100 meters (Criado-Aldeanueva et al., 2006), which is in agreement
566 with the Montemayor-1 paleodepth curve of Pérez-Asensio et al. (2012a).

567 ***6.3.2 Water masses***

568 The benthic and planktonic $\delta^{18}O$ records of the Montemayor-1 core follow very similar
569 patterns and they are in phase with each other (Fig. 9). Similar parallel behaviour is also
570 observed in Ain el Beida (Van der Laan et al., 2005) suggesting the presence of the same water
571 mass throughout the water column on both the Moroccan and Iberian margins. Since this
572 water mass follows the global ocean trend, represented by ODP Site 982 (Fig. 10), we agree
573 with Pérez-Asensio et al. (2012b) that this water mass is likely to have been of Atlantic origin.
574 The similar behaviour between the benthic and planktonic $\delta^{18}O$ records both in Morocco and
575 Spain in combination with a relatively shallow paleodepth of a few hundred meters for both
576 sites suggests the presence of NACW, similar to that existing today on both margins. However,
577 this does not rule out the possibility that MOW was flowing further offshore during this time
578 period.

579 Oxygen isotope data recently recorded at ODP Site U1387 (van der Schee, in prep), probably
580 located at greater depth than the Guadalquivir Basin during the Messinian, has heavier benthic
581 oxygen isotope values than those recorded in the Montemayor-1 core. This could be caused by
582 colder water masses and/or advection of Mediterranean sourced heavy $\delta^{18}O$ water at this site.
583 Colder temperatures suggest a vertical temperature gradient in the water column in the
584 vicinity of the Atlantic-Mediterranean gateways during the Messinian, which might imply
585 absence of MOW. In today's Gulf of Cádiz, due to the nearly constant temperature of MOW,
586 there is currently no vertical temperature gradient at the 500-1500 m depth interval (Criado-
587 Aldeanueva et al., 2006). The presence of a vertical temperature gradient, as has been argued

588 here based on the difference in $\delta^{18}O$ between ODP Site U1387 and the Montemayor-1 core,
589 may imply that MOW was absent in the uppermost Messinian. Other oxygen isotope records
590 at intermediate depths in the northeast Atlantic margins close to the Messinian gateways are
591 needed to reconstruct the vertical temperature and oxygen isotope gradients in the
592 Guadalquivir Basin and Gulf of Cádiz, and address the evolution of MOW in this region.

593 Due to the difference in trend in the benthic $\delta^{18}O$ records of the Montemayor-1 core and Ain el
594 Beida, stated in section 6.3.1, the benthic $\delta^{18}O$ record of the Montemayor-1 core yields
595 different mean values from Ain el Beida and Loulja between 5.9-5.5 Ma (green box in Fig. 10),
596 which coincides with the latest Messinian glacial period (Hodell et al., 2001) and the first
597 stages of the MSC (Roveri et al., 2014). During this time period the benthic $\delta^{18}O$ values of the
598 Montemayor-1 core are higher than at Loulja or Ain el Beida, approaching the North Atlantic
599 values of ODP Site 982, especially during the most prominent glacial cycles TG12, TG14, TG20
600 and TG22 (Fig. 10). This might be the result of a decrease in or cessation of MOW so that cold
601 North Atlantic Intermediate Water could penetrate shallower water depths resulting in a
602 colder and therefore heavier $\delta^{18}O$ signal. This is congruent with the deposition of the lower
603 evaporites and halite in the Mediterranean Basin during this period, indicating at least a very
604 restricted connection between the Atlantic and the Mediterranean with negligible outflow.
605 Were this to be the case however, it is surprising that Ain el Beida does not show the same
606 increase in $\delta^{18}O$ values. An explanation might be that Ain el Beida was located at a slightly
607 shallower depth, or experienced a concurrent shallowing, resulting in the influence of warmer,
608 shallower water.

609 An alternative explanation could be that the influence of heavier oxygen isotope water flowing
610 out of the saline Mediterranean results in heavier $\delta^{18}O$ values in the Guadalquivir Basin
611 between 5.9 and 5.5 Ma. The increasing trend in the benthic $\delta^{18}O$ record may be caused by the
612 advection of increasingly more saline MOW, counteracting the effect of the presumed

613 reduction in outflow as a result of the very restricted connection during these first stages of
614 the MSC. The northward bending of the MOW after exiting the Mediterranean due to Coriolis
615 forcing should explain its greater influence along the Spanish margin relative to Morocco.
616 However, during deposition of halite in the Mediterranean, a complete cessation of MOW at
617 5.60-5.55 Ma is required (Meijer, 2006) while we observe a maximum in oxygen isotope
618 values. Another alternative could be upwelling in the Guadalquivir Basin, bringing deeper,
619 colder waters to the surface during this time period. To be consistent with the lighter oxygen
620 isotope values found at Ain el Beida, this process would have affected Morocco to a smaller
621 degree. However, as indicated by low values of *U. peregrina* (Fig. 9), upwelling influence seems
622 to be very low in this part of the Montemayor-1 record (Pérez-Asensio et al., 2014).

623 For our record in general we can conclude that the sediments of the Montemayor-1 core were
624 not directly influenced by MOW, probably due to its relatively shallow paleodepth, based on
625 the paleodepth curve of Pérez-Asensio et al. (2012a), which infers a maximum paleodepth of
626 450 meters. However, we cannot rule out presence of MOW at greater depths, and the
627 indirect influence of MOW on the Montemayor-1 core mixing with the overlying NACW. This
628 conclusion is in agreement with Pérez-Asensio et al. (2012b) who, based on various lines of
629 evidence, concluded that the sediments of the Montemayor-1 core were only affected by
630 MOW prior to 6.18 Ma. In particular, these authors point out the offset between, and different
631 behaviour of the planktonic and benthic $\delta^{18}O$ records before 6.18 Ma, which they relate to the
632 influence of Mediterranean derived waters at the bottom of the water column. In our record
633 the interval before 6.18 Ma is too short (190 kyr), and the oxygen isotope data points too
634 scarce (20 data points), to come to a conclusive statement as to whether MOW was present or
635 not in this part of the record. A later date for MOW cessation, however, is not incompatible
636 with our data, and would be supported by one of the interpretations of the deviation in
637 benthic isotope record values of the Montemayor-1 core for the 5.9-5.5 Ma period.

638 Unfortunately the resolution of the Montemayor-1 stable isotope records in the lower interval
639 is too low to draw any firm conclusions about the origin of any higher order fluctuations of
640 these records. For example, one of the arguments Pérez-Asensio et al. (2012b) uses for MOW
641 cessation at 6.18 Ma is the benthic oxygen isotope excursion in the Montemayor-1 core at this
642 time (Fig. 9). However, a similar decrease in the benthic $\delta^{18}O$ is seen in the high resolution
643 benthic oxygen isotope record of Ain el Beida (Fig. 9) and in this case is clearly linked to the
644 high amplitude precession minima at times of eccentricity maxima (Krijgsman et al., 2004).
645 Various pronounced minima and lower mean values in the $\delta^{18}O$ are recorded at times of high
646 amplitude insolation maxima during the two eccentricity maxima centered around 6.3 and 6.2
647 Ma (Fig. 9). The 100 kyr eccentricity maxima around 6.2 may therefore also have caused the
648 concurrent abrupt decrease in the benthic oxygen isotope values of the Montemayor-1 core at
649 6.22 Ma, rather than the cessation of MOW. A high resolution study for the Montemayor-1
650 core, together with high resolution oxygen isotope records from other parts of the
651 Guadalquivir Basin, are required to test different interpretations and evaluate better the
652 evolution of Messinian MOW.

653 ## 7. Conclusions

654 A new high-resolution chronostratigraphic age model for the Guadalquivir Basin at the Atlantic
655 end of the Betic corridor has been constructed by tuning cyclic changes in elemental
656 composition of sediments from the Montemayor-1 core to insolation using magneto- and
657 biostratigraphic tie points. This age model spans the late Messinian (6.37-5.33 Ma) and permits
658 comparison of previously published records of stable isotopes and benthic foraminifera with
659 global and regional equivalents. We recognize a gradual change in the nature of the typical
660 fluctuations in geochemical composition of the sediments through the core, which is
661 associated with a gradual change in depositional environment as the basin infilled. The lower
662 part of the core yields alternations of biogenic carbonate layers with beds of terrigenous clay

material. The terrigenous material dilutes the biogenic carbonate during periods of increased river runoff induced by maxima in Northern Hemisphere summer insolation. In the upper interval of the record, the nature of the cycles changes probably as a result of more proximal setting. In this shallow marine environment, sedimentation is dominated by coarser grained terrestrial input. Due to increased erosion rates caused by a loss in vegetation cover during insolation minima, enhanced input of silty detrital sediments dilutes the biogenic carbonate and the clay.

Based on the new age model, the benthic oxygen isotope records correlate well with the previously published records of Ain el Beida, Loulja and ODP Site 982. Glacial stages TG12, TG14, TG20 and TG22 as well as the deglaciation towards TG11 and finally TG9 are clearly expressed. Similar behaviour in the planktonic and benthic oxygen isotope records for Ain el Beida, Loulja and the Montemayor-1 core, together with general trends reflecting open ocean signals, suggest the presence of NACW and no direct influence of MOW on the sediments of the Montemayor-1 record. We recognize an offset between the benthic oxygen isotope records of the Montemayor-1 core and Ain el Beida for the last Messinian glacial period (5.9-5.5 Ma), concurrent with the first stages of the MSC. This might be the result of the decrease/cessation of the MOW in the Gibraltar Strait region, but could also be explained by the presence of more saline MOW or upwelling. Additional high-resolution records from the Atlantic margins near the Gibraltar Strait are needed to reconstruct fully the role and evolution of MOW during the Messinian Salinity Crisis.

687 **Acknowledgements**

688 Jose Noel Perez-Asensio is thanked for providing the stable isotope and benthic foraminifera
689 data sets. All fellow Medgate ESR's, ER and supervisors are thanked for their valuable
690 suggestions and discussions. Francisco Jimenez-Espejo, Tanja Kouwenhoven and two
691 anonymous reviewers are thanked for their critical comments, which greatly improved the
692 manuscript. The research leading to these results has received funding from the People
693 Programme (Marie Curie Actions) of the European Union's Seventh Framework Programme
694 FP7/2007-2013/ under REA Grant Agreement No. 290201 MEDGATE, and from the Guadaltyc
695 project (MINECO, CGL2012-30875). Funding from JCYL project SA263U14 is also acknowledged.

References

Aitchison, J., 1986. The statistical analysis of compositional data. Springer.

Berástegui, X., Banks, C.J., Puig, C., Taberner, C., Waltham, D. and Fernández, M., 1998. Lateral diapiric emplacement of Triassic evaporites at the southern margin of the Guadalquivir Basin, Spain. Geological Society, London, Special Publications, 134(1), 49-68.

Bourillot, R., Vennin, E., Rouchy, J.-M., Blanc-Valleron, M.-M., Caruso, A. and Durlet, C., 2010. The end of the Messinian Salinity Crisis in the western Mediterranean: Insights from the carbonate platforms of south-eastern Spain. Sedimentary Geology, 229(4), 224-253.

Bozzano, G., Kuhlmann, H. and Alonso, B., 2002. Storminess control over African dust input to the Moroccan Atlantic margin (NW Africa) at the time of maxima boreal summer insolation: a record of the last 220 kyr. Palaeogeography, Palaeoclimatology, Palaeoecology, 183(1), 155-168.

Braga, J.C., Martín, J.M., Riding, R., Aguirre, J., Sánchez-Almazo, I.M. and Dinarès-Turell, J., 2006. Testing models for the Messinian salinity crisis: the Messinian record in Almería, SE Spain. Sedimentary Geology, 188, 131-154.

Cerdan, O., Govers, G., Le Bissonnais, Y., Van Oost, K., Poesen, J., Saby, N., Gobin, A., Vacca, A., Quinton, J. and Auerswald, K., 2010. Rates and spatial variations of soil erosion in Europe: a study based on erosion plot data. Geomorphology, 122(1), 167-177.

CIESM, 2008. The Messinian salinity crisis from mega-deposits to microbiology. in: F. Briand (Ed.), A consensus report, in 33ème CIESM Workshop Monographs, 33CIESM, 16, bd de Suisse, MC-98000, Monaco(33), 1-168.

Criado-Aldeanueva, F., García-Lafuente, J., Vargas, J.M., Del Río, J., Vazquez, A., Reul, A. and Sánchez, A., 2006. Distribution and circulation of water masses in the Gulf of Cadiz from in situ observations. Deep Sea Research Part II: Topical Studies in Oceanography, 53(11), 1144-1160.

Damnati, B., Petit-Maire, N., Fontugne, M., Meco, J. and Williamson, D., 1996. Quaternary palaeoclimates in the eastern Canary Islands. Quaternary International, 31, 37-46.

Davis, J.C. and Sampson, R.J., 2002. Statistics and data analysis in geology. Wiley New York.

Dean, R. and Dixon, W., 1951. Simplified statistics for small numbers of observations. Analytical Chemistry, 23(4), 636-638.

Dennison, J.M. and Hay, W.W., 1967. Estimating the Needed Sampling Area for Subaquatic Ecologic Studies. Journal of Paleontology, 41(3), 706-708.

Fatela, F. and Taborda, R., 2002. Confidence limits of species proportions in microfossil assemblages. Marine Micropaleontology, 45(2), 169-174.

García-Castellanos, D., Fernandez, M. and Torné, M., 2002. Modeling the evolution of the Guadalquivir foreland basin (southern Spain). Tectonics, 21(3), 9-1-9-17.

González-Delgado, J.A., Civis, J., Dabrio, C.J., Goy, J.L., Ledesma, S., Pais, J., Sierro, F.J. and Zazo, C., 2004. Cuenca del Guadalquivir. Geología de España: Madrid, Sociedad Geológica Española, Instituto Geológico y Minero Español, 543-550.

Hammer, Ø., Harper, D. and Ryan, P., 2001. PAST: Paleontological Statistics Software Package for education and data analysis. Palaeontolia Electronica 4.

Harvey, A.M., Wigand, P.E. and Wells, S.G., 1999. Response of alluvial fan systems to the late Pleistocene to Holocene climatic transition: contrasts between the margins of pluvial Lakes Lahontan and Mojave, Nevada and California, USA. Catena, 36(4), 255-281.

Higueras, P., Oyarzun, R., Iraizoz, J., Lorenzo, S., Esbrí, J. and Martínez-Coronado, A., 2012. Low-cost geochemical surveys for environmental studies in developing countries: Testing a field portable XRF instrument under quasi-realistic conditions. Journal of Geochemical Exploration, 113, 3-12.

745 Hodell, D., Crowhurst, S., Skinner, L., Tzedakis, P.C., Margari, V., Channell, J.E., Kamenov, G.,
746 Maclachlan, S. and Rothwell, G., 2013. Response of Iberian Margin sediments to orbital
747 and suborbital forcing over the past 420 ka. Paleoceanography, 28(1), 185-199.
748 Hodell, D.A., Curtis, J.H., Sierro, F.J. and Raymo, M.E., 2001. Correlation of late Miocene to
749 early Pliocene sequences between the Mediterranean and North Atlantic.
750 Paleoceanography, 16(2), 164-178.
751 Hsü, K., Ryan, W. and Cita, M., 1973. Late Miocene desiccation of the Mediterranean. Nature,
752 242(5395), 240-244.
753 Iribarren, L., Vergés, J. and Fernández, M., 2009. Sediment supply from the Betic–Rif orogen to
754 basins through Neogene. Tectonophysics, 475(1), 68-84.
755 Jansen, J., Van der Gaast, S., Koster, B. and Vaars, A., 1998. CORTEX, a shipboard XRF-scanner
756 for element analyses in split sediment cores. Marine Geology, 151(1), 143-153.
757 Jiménez-Moreno, G., Pérez-Asensio, J.N., Larrasoaña, J.C., Aguirre, J., Civis, J., Rivas-Carballo,
758 M.R., Valle-Hernández, M.F. and González-Delgado, J.A., 2013. Vegetation, sea-level,
759 and climate changes during the Messinian salinity crisis. Geological Society of America
760 Bulletin, 125(3-4), 432-444.
761 Kaboth, S., Bahr, A., Reichart, G.-J., Jacobs, B. and Lourens, L.J., this issue. New insights into
762 Upper MOW variability over the last 150 ka from IODP 339 Site U1386 in the Gulf of
763 Cadiz. Global and Planetary Change.
764 Kalnicky, D.J. and Singhvi, R., 2001. Field portable XRF analysis of environmental samples.
765 Journal of hazardous materials, 83(1), 93-122.
766 Krijgsman, W., Hilgen, F.J., Raffi, I., Sierro, F.J. and Wilson, D.S., 1999. Chronology, causes and
767 progression of the Messinian salinity crisis. Nature, 400(6745), 652-655.
768 Krijgsman, W. and Langereis, C., 2000. Magnetostratigraphy of the Zobzit and Koudiat Zarga
769 sections (Taza-Guercif basin, Morocco): implications for the evolution of the Rifian
770 Corridor. Marine and Petroleum Geology, 17(3), 359-371.
771 Krijgsman, W., Fortuin, A., Hilgen, F. and Sierro, F., 2001. Astrochronology for the Messinian
772 Sorbas basin (SE Spain) and orbital (precessional) forcing for evaporite cyclicity.
773 Sedimentary Geology, 140(1), 43-60.
774 Krijgsman, W., Gaboardi, S., Hilgen, F., Iaccarino, S., De Kaenel, E. and Van der Laan, E., 2004.
775 Revised astrochronology for the Ain el Beida section (Atlantic Morocco): no glacio-
776 eustatic control for the onset of the Messinian Salinity Crisis. Stratigraphy, 1(1), 87-
777 101.
778 Krijgsman, W. and Meijer, P.T., 2008. Depositional environments of the Mediterranean “Lower
779 Evaporites” of the Messinian salinity crisis: constraints from quantitative analyses.
780 Marine Geology, 253(3), 73-81.
781 Larrasoaña, J.C., González-Delgado, J.A., Civis, J., Sierro, F.J., Alonso-Gavilán, G. and Pais, J.,
782 2008. Magnetobiostratigraphic dating and environmental magnetism of Late Neogene
783 marine sediments recovered at the Huelva-1 and Montemayor-1 boreholes (lower
784 Guadalquivir basin, Spain). Geo-Temas, 10, 1175-1178.
785 Larrasoaña, J.C., Liu, Q., Hu, P., Roberts, A.P., Mata, P., Civis, J., Sierro, F.J. and Pérez-Asensio,
786 J.N., 2014. Paleomagnetic and paleoenvironmental implications of magnetofossil
787 occurrences in late Miocene marine sediments from the Guadalquivir Basin, SW Spain.
788 Frontiers in microbiology, 5.
789 Laskar, J., Robutel, P., Joutel, F., Gastineau, M., Correia, A. and Levrard, B., 2004. A long-term
790 numerical solution for the insolation quantities of the Earth. Astronomy &
791 Astrophysics, 428(1), 261-285.
792 Lofi, J., Voelker, A.H.L., Ducassou, E., Hernández-Molina, F.J., Sierro, F.J., Bahr, A., Galvani, A.,
793 Lourens, L.J., Pardo-Igúzquiza, E., Rodríguez-Tovar, F.J. and Williams, T., this issue.
794 Quaternary record in the Gulf of Cádiz and Portuguese Contourite Depositional
795 Systems. Global and Planetary Change.

796 Lourens, L.J., Hilgen, F.J., Laskar, J., Shackleton, N.J. and Wilson, D., 2004. The Neogene Period.
797 In: F.M. Gradstein, Ogg, J.G., Smith, A.G. (Ed.), A Geologic Time Scale 2004. Cambridge
798 University Press, Cambridge, pp. 409-440.
799 Martín, J.M., Puga-Bernabéu, Á., Aguirre, J. and Braga, J.C., 2014. Miocene Atlantic-
800 Mediterranean seaways in the Betic Cordillera (southern Spain). Revista de la Sociedad
801 Geológica de España, 27, 1.
802 McCave, I., Manighetti, B. and Robinson, S., 1995. Sortable silt and fine sediment
803 size/composition slicing: Parameters for palaeocurrent speed and palaeoceanography.
804 Paleoceanography, 10(3), 593-610.
805 McCave, I. and Hall, I., 2006. Size sorting in marine muds: Processes, pitfalls, and prospects for
806 paleoflow-speed proxies. Geochemistry, Geophysics, Geosystems, 7(10).
807 Meijer, P.T., 2006. A box model of the blocked-outflow scenario for the Messinian Salinity
808 Crisis. Earth and Planetary Science Letters, 248(1–2), 486-494.
809 Milankovitch, M., 1941. History of radiation on the Earth and its use for the problem of the ice
810 ages. K. Serb. Akad. Beogr.
811 Moreno, A., Targarona, J., Henderiks, J., Canals, M., Freudenthal, T. and Meggers, H., 2001.
812 Orbital forcing of dust supply to the North Canary Basin over the last 250kyr.
813 Quaternary Science Reviews, 20(12), 1327-1339.
814 Pérez-Asensio, J.N., Aguirre, J., Schmiedl, G. and Civis, J., 2012a. Messinian paleoenvironmental
815 evolution in the lower Guadalquivir Basin (SW Spain) based on benthic foraminifera.
816 Palaeogeography, Palaeoclimatology, Palaeoecology, 326, 135-151.
817 Pérez-Asensio, J.N., Aguirre, J., Schmiedl, G. and Civis, J., 2012b. Impact of restriction of the
818 Atlantic-Mediterranean gateway on the Mediterranean Outflow Water and eastern
819 Atlantic circulation during the Messinian. Paleoceanography, 27(3).
820 Pérez-Asensio, J.N., Aguirre, J., Jimenez-Moreno, G., Schmiedl, G. and Civis, J., 2013.
821 Glacioeustatic control on the origin and cessation of the Messinian salinity crisis.
822 Global and Planetary Change, 111, 1-8.
823 Pérez-Asensio, J.N., Aguirre, J., Schmiedl, G. and Civis, J., 2014. Messinian productivity changes
824 in the northeastern Atlantic and their relationship to the closure of the Atlantic–
825 Mediterranean gateway: implications for Neogene palaeoclimate and
826 palaeoceanography. Journal of the Geological Society, 171(3), 389-400.
827 Pla-Pueyo, S., Viseras, C., Candy, I., Soria, J.M., García-García, F. and Schreve, D., 2015. Climatic
828 control on palaeohydrology and cyclical sediment distribution in the Plio-Quaternary
829 deposits of the Guadix Basin (Betic Cordillera, Spain). Quaternary International.
830 Richter, T.O., Van der Gaast, S., Koster, B., Vaars, A., Gieles, R., de Stigter, H.C., De Haas, H. and
831 van Weering, T.C., 2006. The Avaatech XRF Core Scanner: technical description and
832 applications to NE Atlantic sediments. Geological Society, London, Special Publications,
833 267(1), 39-50.
834 Riding, R., Braga, J.C., Martín, J.M. and Sánchez-Almazo, I.M., 1998. Mediterranean Messinian
835 Salinity Crisis: constraints from a coeval marginal basin, Sorbas, southeastern Spain.
836 Marine Geology, 146(1), 1-20.
837 Rorabacher, D.B., 1991. Statistical treatment for rejection of deviant values: critical values of
838 Dixon's" Q" parameter and related subrange ratios at the 95% confidence level.
839 Analytical Chemistry, 63(2), 139-146.
840 Roveri, M., Flecker, R., Krijgsman, W., Lofi, J., Lugli, S., Manzi, V., Sierro, F.J., Bertini, A.,
841 Camerlenghi, A. and De Lange, G., 2014. The Messinian Salinity Crisis: Past and future
842 of a great challenge for marine sciences. Marine Geology, 352, 25-58.
843 Rowe, H., Hughes, N. and Robinson, K., 2012. The quantification and application of handheld
844 energy-dispersive x-ray fluorescence (ED-XRF) in mudrock chemostratigraphy and
845 geochemistry. Chemical Geology, 324, 122-131.
846 Ryan, W.B., 2009. Decoding the Mediterranean salinity crisis. Sedimentology, 56(1), 95-136.

847 Salvany, J.M., Larrasoaña, J.C., Mediavilla, C. and Rebollo, A., 2011. Chronology and tectono-
848 sedimentary evolution of the Upper Pliocene to Quaternary deposits of the lower
849 Guadalquivir foreland basin, SW Spain. Sedimentary Geology, 241(1), 22-39.
850 Sanz de Galdeano, C.M. and Vera, J.A., 1992. Stratigraphic record and palaeogeographical
851 context of the Neogene basins in the Betic Cordillera, Spain. Basin Research, 4(1), 21-
852 36.
853 Shackleton, N., 1974. Attainment of isotopic equilibrium between ocean water and the
854 benthonic foraminifera genus Uvigerina: isotopic changes in the ocean during the last
855 glacial.
856 Shackleton, N., Hall, M. and Pate, D., 1995. 15. Pliocene stable isotope stratigraphy of Site 846,
857 Proc. Ocean Drill. Program Sci. Results, pp. 337-355.
858 Sierro, F.J., Flores, J.A. and Civis, J., 1993. Late Miocene globorotaliid event-stratigraphy and
859 biogeography in the NE-Atlantic and Mediterranean. Marine Micropaleontology, 21(1),
860 143-167.
861 Sierro, F.J., Delgado, J.A.G., Flores, C.D.J. and Civis, J., 1996. S4 Late Neogene depositional
862 sequences in the foreland basin of Guadalquivir (SW Spain), Tertiary Basins of Spain:
863 The stratigraphic record of crustal kinematics, pp. 339.
864 Sierro, F.J., Ledesma, S., Flores, J.A., Torrescusa, S. and Martinez del Olmo, W., 2000. Sonic and
865 gamma-ray astrochronology: Cycle to cycle calibration of Atlantic climatic records to
866 Mediterranean sapropels and astronomical oscillations. Geology, 28(8), 695-698.
867 Sierro, F.J., Hilgen, F.J., Krijgsman, W. and Flores, J.A., 2001. The Abad composite (SE Spain): a
868 Messinian reference section for the Mediterranean and the APTS. Palaeogeography,
869 Palaeoclimatology, Palaeoecology, 168(1), 141-169.
870 Simon, D. and Meijer, P., 2015. Dimensions of the Atlantic-Mediterranean connection that
871 caused the Messinian Salinity Crisis. Marine Geology, 364, 53-64.
872 Strasser, A., Hilgen, F.J. and Heckel, P.H., 2006. Cyclostratigraphy–concepts, definitions, and
873 applications. Newsletters on Stratigraphy, 42(2), 75-114.
874 Tjallingii, R., Röhl, U., Kölling, M. and Bickert, T., 2007. Influence of the water content on X-ray
875 fluorescence core-scanning measurements in soft marine sediments. Geochemistry,
876 Geophysics, Geosystems, 8(2).
877 USEPA, 2006. XRF technologies for measuring trace elements in soil and sediment: Oxford X-
878 Met 3000TX XRF Analyzer. Innovative Technology Verification Report.
879 Van Assen, E., Kuiper, K., Barhoun, N., Krijgsman, W. and Sierro, F., 2006. Messinian
880 astrochronology of the Melilla Basin: stepwise restriction of the Mediterranean–
881 Atlantic connection through Morocco. Palaeogeography, Palaeoclimatology,
882 Palaeoecology, 238(1), 15-31.
883 Van der Laan, E., Gaboardi, S., Hilgen, F. and Lourens, L., 2005. Regional climate and glacial
884 control on high-resolution oxygen isotope records from Ain el Beida (latest Miocene,
885 northwest Morocco): A cyclostratigraphic analysis in the depth and time domain.
886 Paleoceanography, 20(1).
887 Van der Laan, E., Snel, E., De Kaenel, E., Hilgen, F. and Krijgsman, W., 2006. No major
888 deglaciation across the Miocene-Pliocene boundary: Integrated stratigraphy and
889 astronomical tuning of the Loulja sections (Bou Regreg area, NW Morocco).
890 Paleoceanography, 21(3).
891 Van der Laan, E., Hilgen, F., Lourens, L., De Kaenel, E., Gaboardi, S. and Iaccarino, S., 2012.
892 Astronomical forcing of Northwest African climate and glacial history during the late
893 Messinian (6.5–5.5 Ma). Palaeogeography, Palaeoclimatology, Palaeoecology, 313,
894 107-126.
895 von Suchodoletz, H., Fuchs, M. and Zöller, L., 2008. Dating Saharan dust deposits on Lanzarote
896 (Canary Islands) by luminescence dating techniques and their implication for
897 palaeoclimate reconstruction of NW Africa. Geochemistry, Geophysics, Geosystems,
898 9(2).

von Suchodoletz, H., Oberhänsli, H., Hambach, U., Zöller, L., Fuchs, M. and Faust, D., 2010. Soil moisture fluctuations recorded in Saharan dust deposits on Lanzarote (Canary Islands) over the last 180ka. Quaternary Science Reviews, 29(17), 2173-2184.

Figure captions:

Figure 1: Schematic geological map of the Gibraltar Strait region with the Neogene basins and the Betic and Rif Orogen. The location of the Montemayor-1 core as well as ODP Leg 339 drill sites and key Messinian sections are shown. The overview map in the upper right corner shows the locations of the Betic and Riffian corridors.

Figure 2: Left: Tortonian-Zanclean magnetostratigraphic chrons and biostratigraphic events of the GTS (Lourens et al., 2004). Numbers denote planktonic foraminiferal events of Sierro et al. (1993). Middle: previously published magnetostratigraphic and biostratigraphic results for the Montemayor-1 core (Larrasoaña et al., 2008) with their relation to the GTS. The lithology column shows from bottom to top the Calcarenita de Niebla formation, Arcillas de Gibraleón formation, Arenas de Huelva formation and Arenas de Bonares formation, respectively. The small black dots represent the glauconite layers at 252 and 60 mcd. Black arrows indicate the part of the borehole addressed in this study. Right: PC1 and PC2, PC1L and PC1U data (black) with their 3 point moving average (red/green/brown/gold). Note the excellent agreement between the original data and the 3 point moving average. In subsequent figures only the 3 point moving average will be shown.

Figure 3: Correlation curves for Calcium, Silicon, Titanium, Strontium, Zirconium and Rubidium measured by the WDS XRF vs. the NITON handheld XRF.

Figure 4: Element concentrations in percentages for the individual elements used in this study.

Figure 5: Loadings of the Principal Components PC1 (top, left), PC2 (top, right), PC1U (bottom, left) and PC1L (bottom, right).

Figure 6: PC1, PC1U, PC1L (all 3 point moving average) and $\delta^{18}O$ (Pérez-Asensio et al., 2013) records in the depth domain (left) converted to a cyclostratigraphic age model (right) using, the insolation, E+T-P and eccentricity (blue) curve (middle). Nomenclature of glacial stages is after Shackleton et al. (1995). *G.m.* is influx of *Globorotalia menardii* sin*, 4 is* bio-event 4 of Sierro et al. (1993), i.e. coiling change of *Neogloboquadrina acostaensis.* The interval with uncertainty in phase relation is shown with dashed lines. In the lithology column (far left) the change from Clays (light grey) to sands (dark grey) is shown, with the glauconite layer (black dots).

Figure 7: Abundance of *Globorotalia margaritae* (blue) and *Globorotalia menardii* sin (red) including 95% confidence interval, and percentage of *Neogloboquadrina acostaensis* species that is sinistral (green), with indications of the core depth for the associated bio-events.

Figure 8: Cross correlation of PC1U and UP10 for a random set of samples of the Montemayor-1 core, including a linear fit.

Figure 9: (a) insolation (yellow) and eccentricity curve (blue), (b) PC1, (c) PC2, (d) relative abundance (%) of *Uvigerina peregrina s.l.*, (e) relative abundance (%) of *Brizalina spathulata,* (f) planktonic and (g) benthic $\delta^{18}O$ record, (h) benthic $\delta^{18}O$ of Ain el Beida (Krijgsman et al., 2004; red) and Loulja (Van der Laan et al., 2006; orange) and (k) the benthic $\delta^{18}O$ record of ODP Leg 982 (Hodell et al., 2001). For all records, except $\delta^{18}O$ of ODP Leg 982, both the original data (thin) and a three point average (thick) are shown. All the records of the Montemayor-1 core are (re-)dated using the cyclostratigraphic age model from this paper. Correlations for the upper part (small dash) are shown, see text for further explanation. Glacial stages (wide dash) and Miocene-Pliocene boundary are put in for reference.

Figure 10: Direct comparison between benthic $\delta^{18}O$ records of the Montemayor-1 core (black), Ain el Beida (Krijgsman et al., 2004; red), Loulja (Van der Laan et al., 2006; orange) and ODP Leg 982 (Hodell et al., 2001; blue). Green box indicates period of deviation between

949 Montemayor and Ain el Beida/Loulja oxygen isotope values, see section 6.3.2. Glacial stages

950 (wide dash) and Miocene-Pliocene boundary are put in for reference.

Figure 1

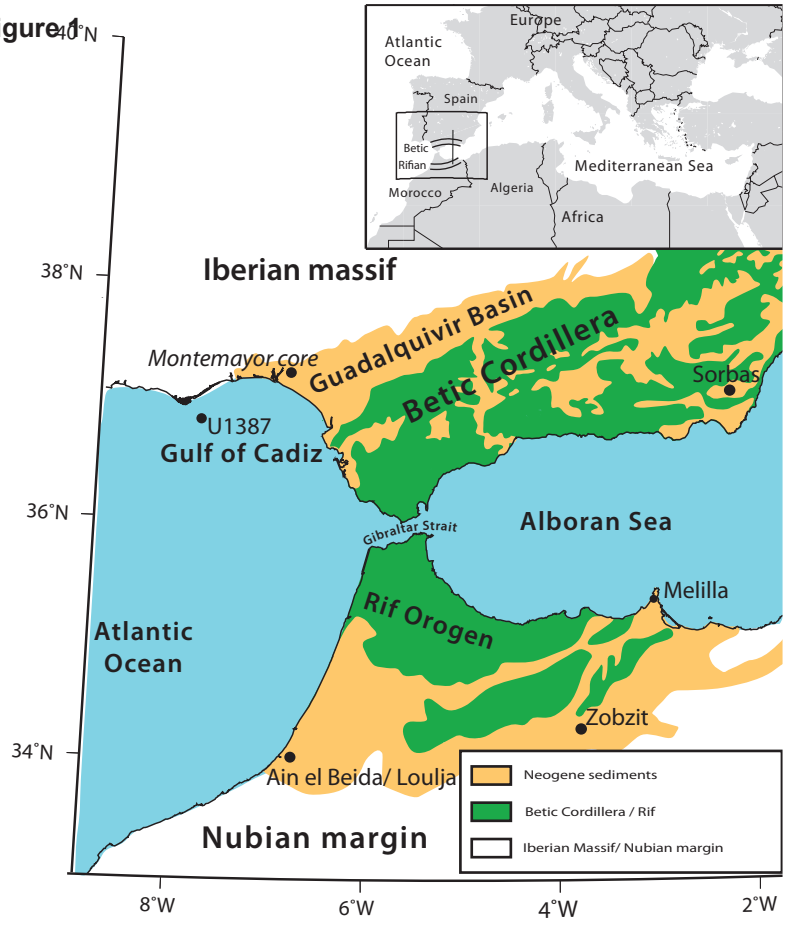
Europe
Atlantic Ocean
Spain
Betic
Rifian
Morocco
Algeria
Mediterranean Sea
Africa
40°N
38°N
36°N
34°N
8°W
6°W
4°W
2°W
Iberian massif
Guadalquivir Basin
Betic Cordillera
Montemayor core
Sorbas
U1387
Gulf of Cadiz
Alboran Sea
Gibraltar Strait
Melilla
Rif Orogen
Atlantic Ocean
Zobzit
Ain el Beida/ Loulja
Nubian margin
Neogene sediments
Betic Cordillera / Rif
Iberian Massif/ Nubian margin

Figure 2

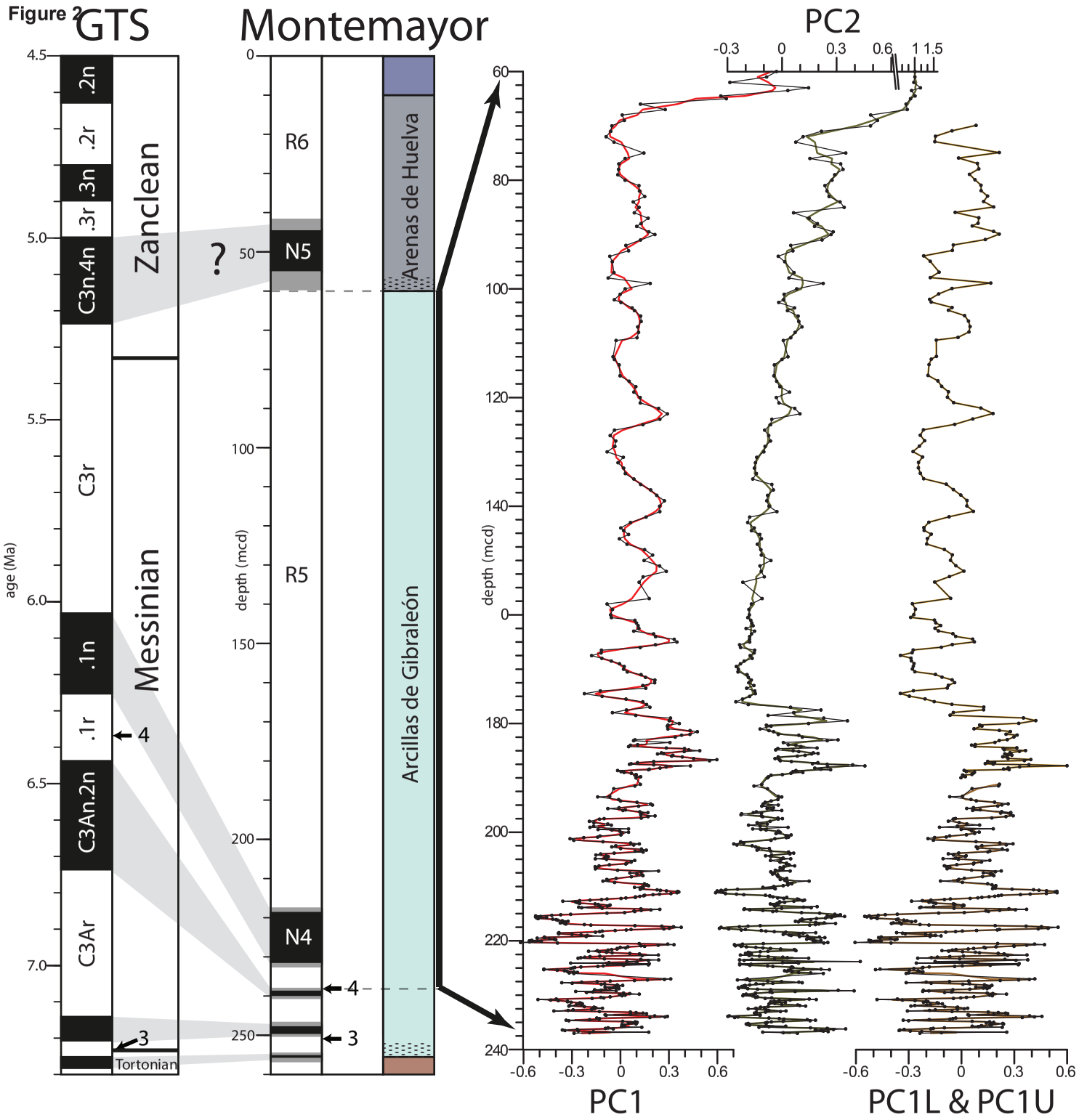
GTS
Montemayor
PC2
age (Ma)
depth (mcd)
.2n
.2r
.3n
.3r
C3n.4n
C3r
.1n
.1r
C3An.2n
C3Ar
Zanclean
Messinian
Tortonian
?
R6
N5
R5
N4
Arenas de Huelva
Arcillas de Gibraleón
4
3
PC1
PC1L & PC1U

Figure 3

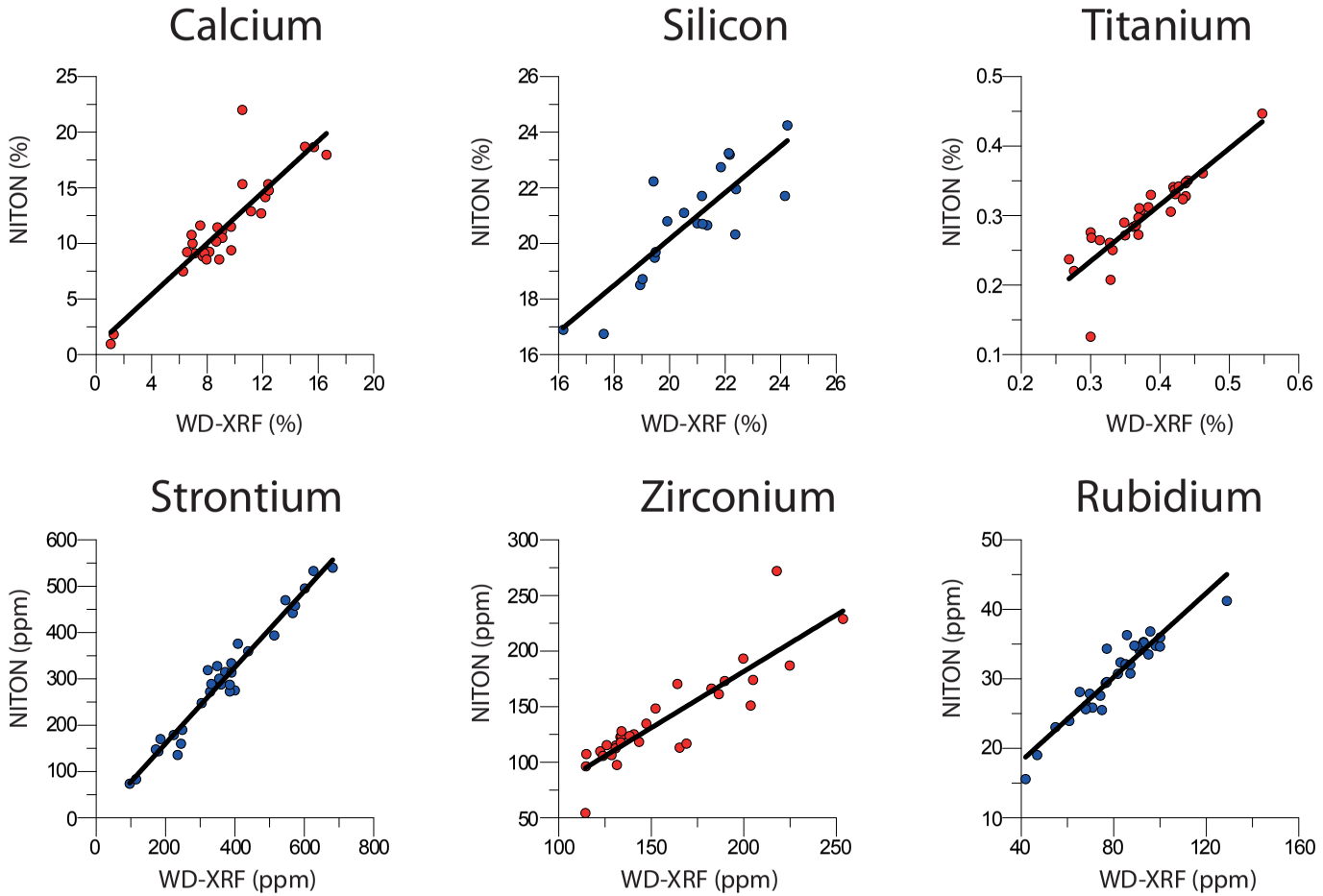
Calcium
NITON (%)
WD-XRF (%)
Silicon
NITON (%)
WD-XRF (%)
Titanium
NITON (%)
WD-XRF (%)
Strontium
NITON (ppm)
WD-XRF (ppm)
Zirconium
NITON (ppm)
WD-XRF (ppm)
Rubidium
NITON (ppm)
WD-XRF (ppm)

Figure 4

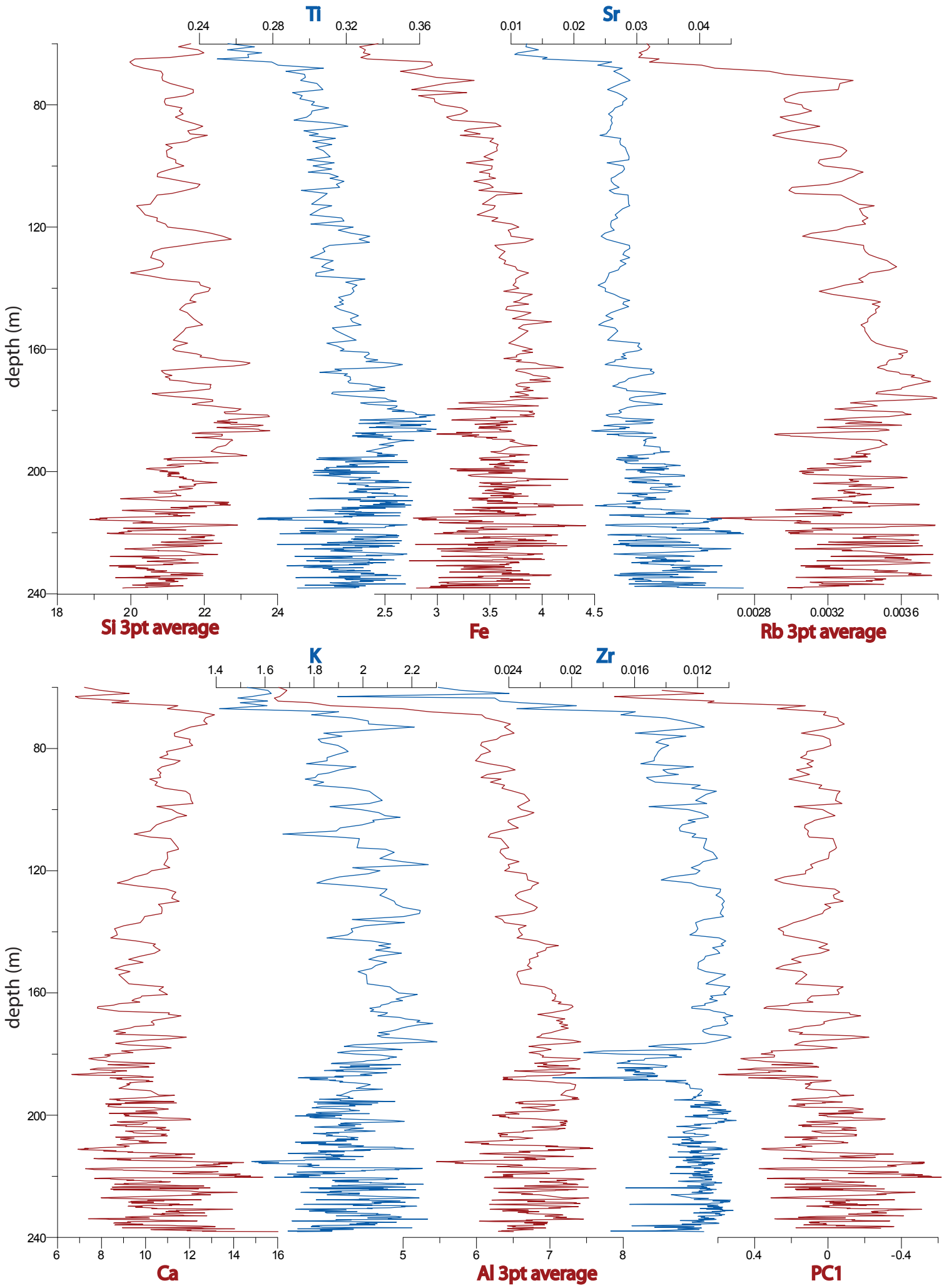
Ti
0.24
0.28
0.32
0.36
Sr
0.01
0.02
0.03
0.04
depth (m)
80
120
160
200
240
18
20
22
24
Si 3pt average
2.5
3
3.5
4
4.5
Fe
0.0028
0.0032
0.0036
Rb 3pt average
K
1.4
1.6
1.8
2
2.2
Zr
0.024
0.02
0.016
0.012
6
8
10
12
14
16
Ca
5
6
7
8
Al 3pt average
0.4
0
-0.4
PC1

Figure 5

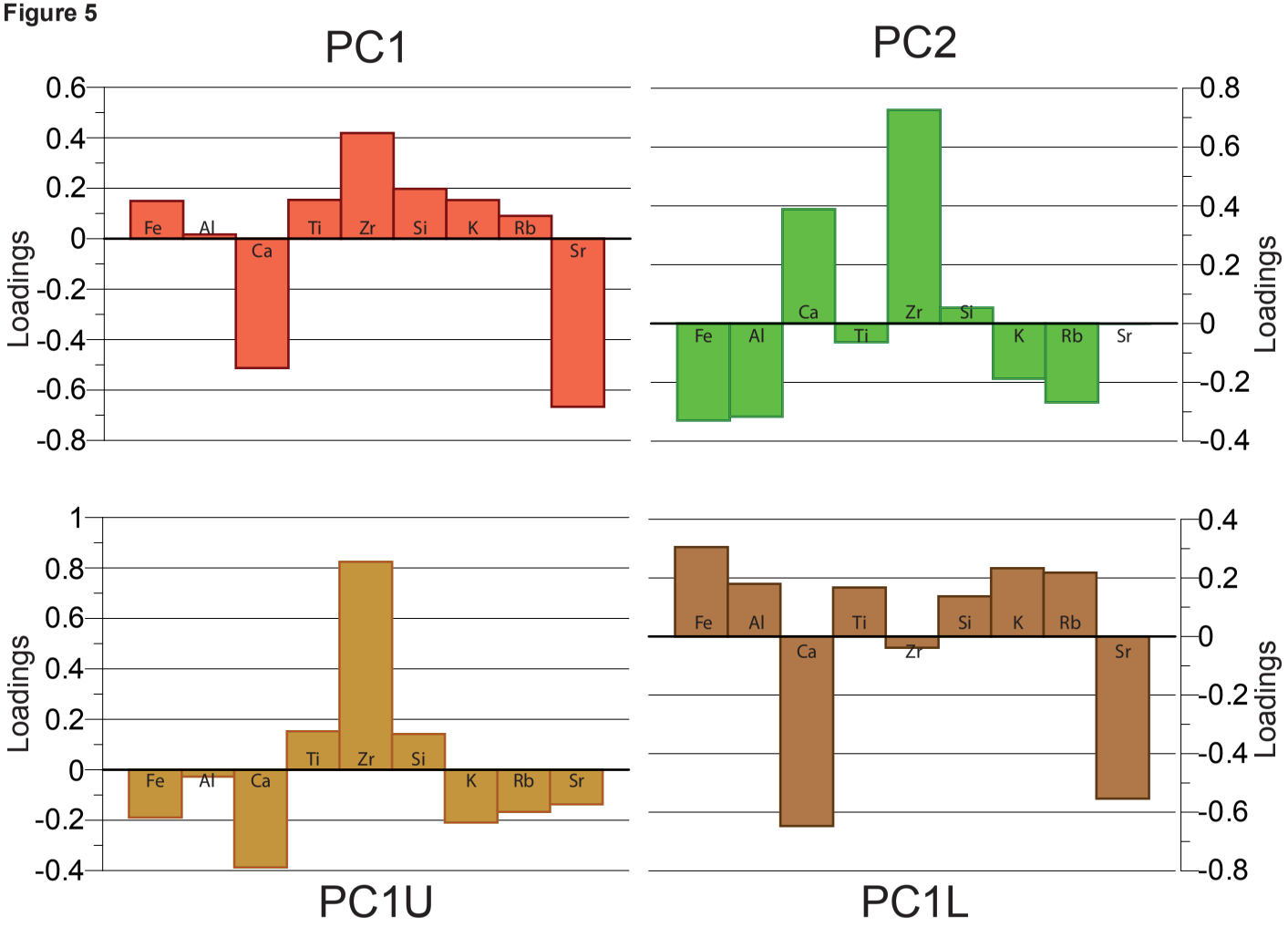
PC1
PC2
Loadings
0.6
0.4
0.2
0
-0.2
-0.4
-0.6
-0.8
Fe
Al
Ca
Ti
Zr
Si
K
Rb
Sr
0.8
1
PC1U
PC1L

Figure 6

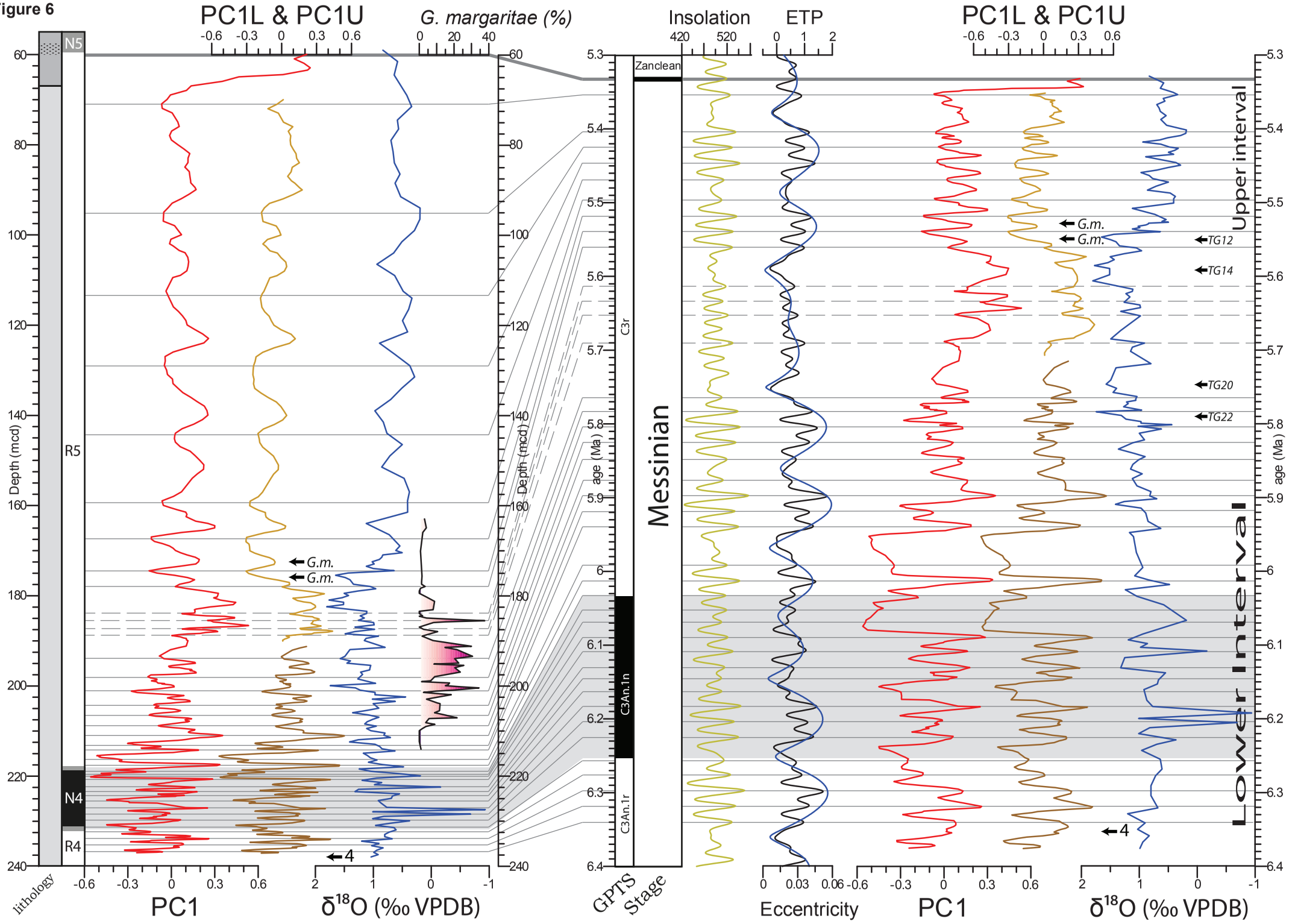
PC1L & PC1U
G. margaritae (%)
Insolation
ETP
PC1L & PC1U
N5
R5
N4
R4
Depth (mcd)
G.m.
G.m.
4
Zanclean
C3r
C3An.1n
C3An.1r
Messinian
age (Ma)
Upper interval
Lower Interval
G.m.
G.m.
TG12
TG14
TG20
TG22
4
lithology
PC1
δ18O (‰ VPDB)
GPTS
Stage
Eccentricity
PC1
δ18O (‰ VPDB)

Figure 7

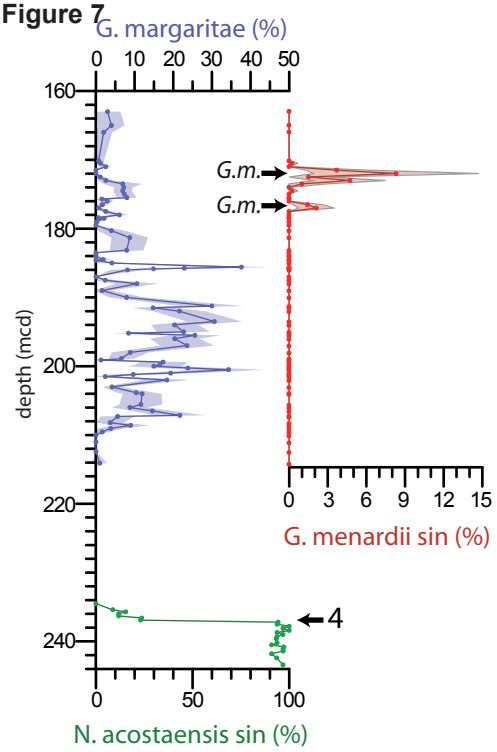
G. margaritae (%)
0 10 20 30 40 50
160
180
200
220
240
depth (mcd)
G.m.
G.m.
0 3 6 9 12 15
G. menardii sin (%)
4
0 50 100
N. acostaensis sin (%)

Figure 8

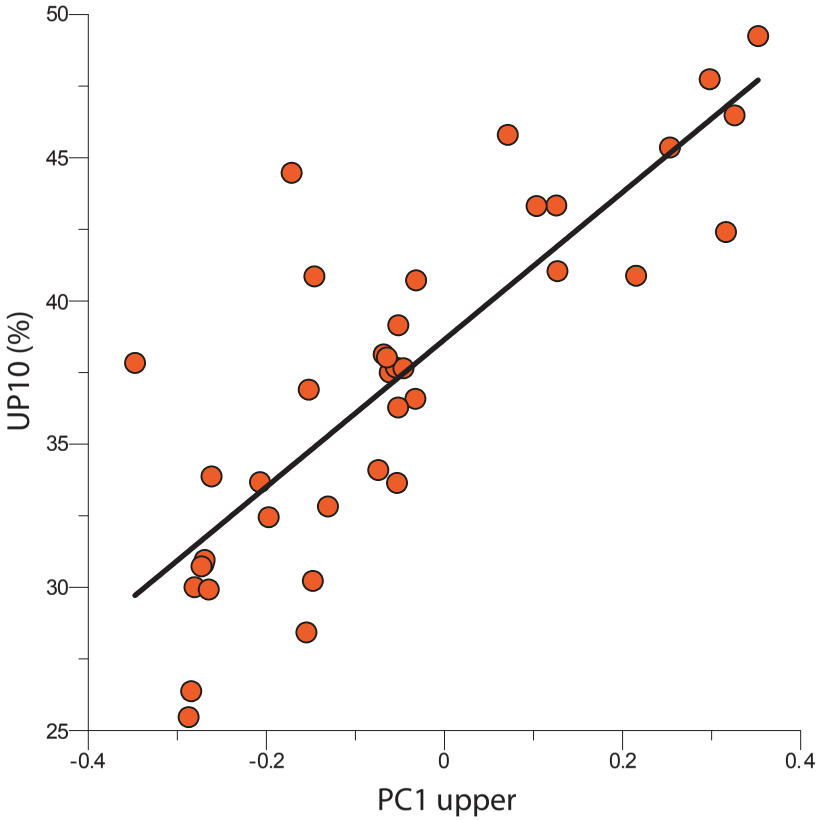

Figure 9

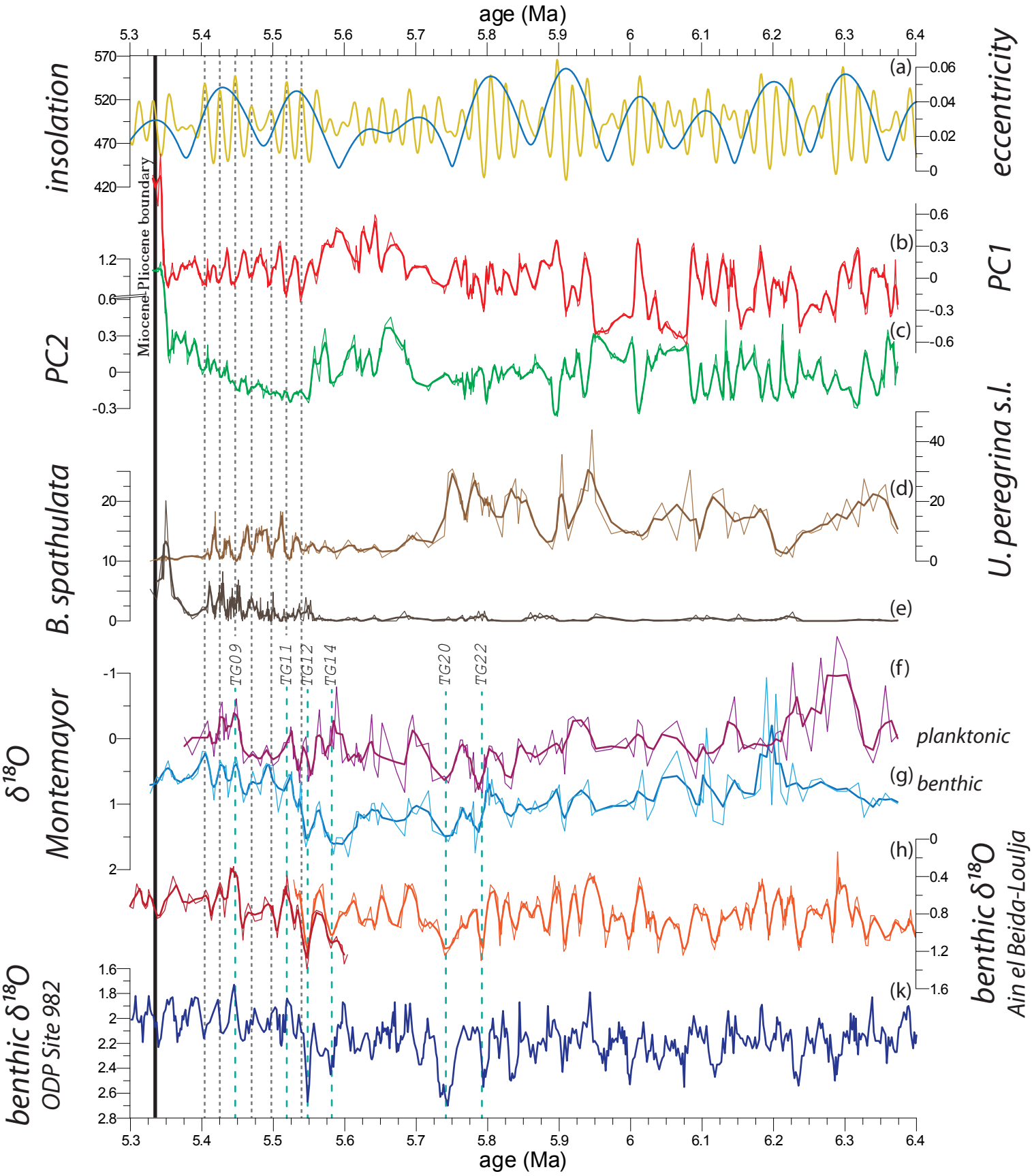
age (Ma)
5.3
5.4
5.5
5.6
5.7
5.8
5.9
6
6.1
6.2
6.3
6.4
insolation
570
520
470
420
(a)
eccentricity
0.06
0.04
0.02
0
Miocene-Pliocene boundary
PC2
1.2
0.6
0.3
0
-0.3
(b)
(c)
PC1
0.6
0.3
0
-0.3
-0.6
B. spathulata
20
10
0
(d)
(e)
U. peregrina s.l.
40
20
0
TG09
TG11
TG12
TG14
TG20
TG22
δ18O Montemayor
-1
0
1
2
(f)
planktonic
(g)
benthic
(h)
benthic δ18O Ain el Beida-Loulja
0
0.4
0.8
1.2
1.6
benthic δ18O ODP Site 982
1.6
1.8
2
2.2
2.4
2.6
2.8
(k)
age (Ma)

Figure 10

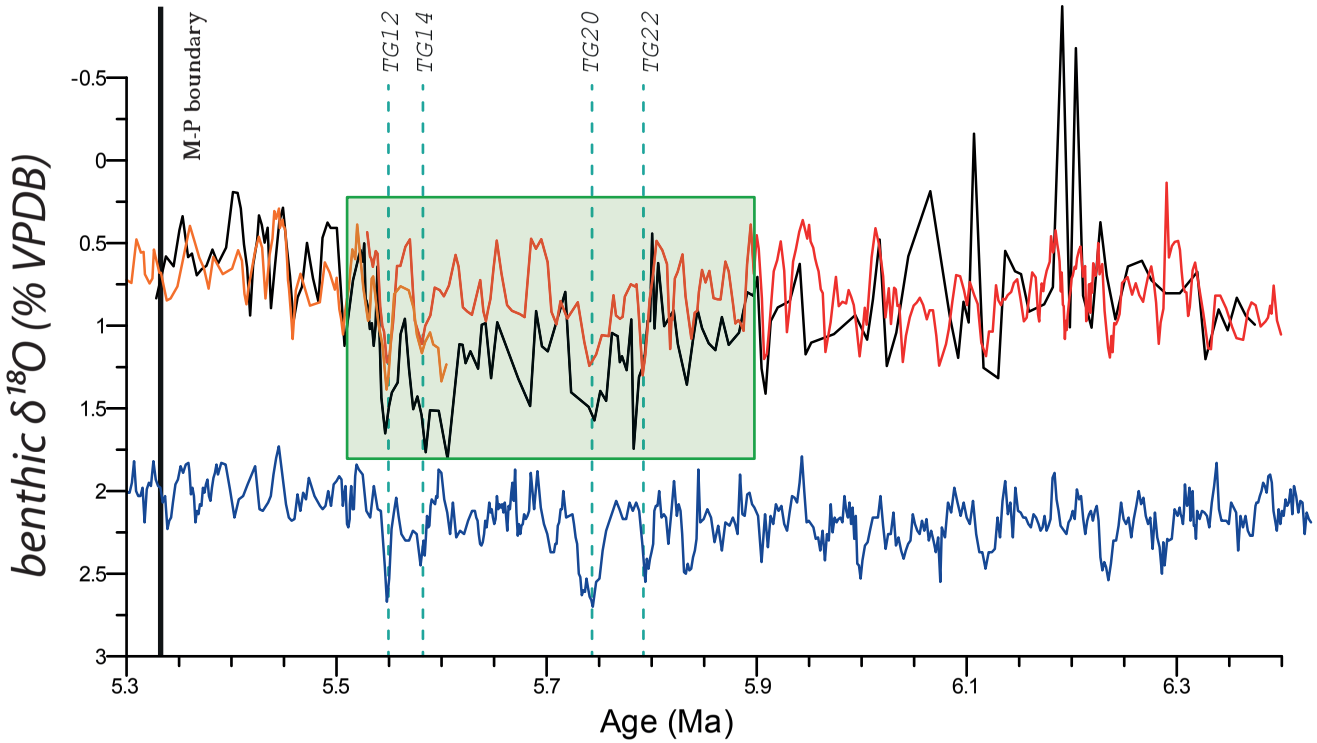
M-P boundary
TG12
TG14
TG20
TG22
benthic δ18O (‰ VPDB)
-0.5
0
0.5
1
1.5
2
2.5
3
5.3
5.5
5.7
5.9
6.1
6.3
Age (Ma)

Table 1: The eigenvalues and variances of the Principal Components

PC	Eigenvalue	% variance	cumulative variance
1	0.0580	45.26	45.26
2	0.0494	38.61	83.87
3	0.0097	7.59	91.46
4	0.0040	3.12	94.58
5	0.0025	1.93	96.51
6	0.0020	1.60	98.10
7	0.0012	0.91	99.01
8	0.0006	0.43	99.44
9	0.0005	0.39	99.84
10	0.0002	0.16	100.00
11	0.0000	0.00	100.00

Supplementary Material for on-line publication only

Click here to download Supplementary Material for on-line publication only: supplementary data.xlsx